

3.1 Introduction

In recent years, InGaAsN/GaAs lasers have shown a great deal of promise as a low cost alternative for directly-modulated 1.3 μ m InP-based devices for use in 10Gb Ethernet, storage area networks, high performance computer clusters and access network applications. The introduction of small quantities of nitrogen into InGaAs quantum wells makes it possible to produce longer wavelength devices suitable for telecommunication systems, which use low cost GaAs substrates. The InGaAsN/GaAs material system has a large band offset, resulting in lasers with a high T_0 (266K [1]) and a small variation of lasing wavelength with temperature (\sim 0.5nm/K). This makes them suitable for uncooled applications. The 1.3 μ m edge-emitting dilute nitride lasers measured in this thesis have achieved a 3dB modulation bandwidth of 17GHz at 298K and can be directly modulated up to 10Gb/s at heatsink temperatures as high as 383K [1].

The performance of dilute nitride devices has improved greatly over the last few years, but further improvements in their long-term reliability are still required to realise their full potential as low-cost sources. An important aspect of improving device performance and achieving higher reliability lies in thermal management and understanding the thermal performance of such devices. In order to accomplish this, accurate simulation tools are required to allow these important aspects to be better

understood. Predictive simulation tools can also be of great benefit for device optimisation.

The development and application of simulation tools requires a wide range of material and device parameters to be known. One of the most important parameters for an optoelectronic device is the optical gain. In the development of uncooled devices, which operate over a wide temperature range (a clearly identified target market for dilute nitride laser diodes), the dependence of the optical gain on temperature is especially important. Whilst many material parameters needed to theoretically calculate the gain are available in the literature, the accurate calibration of a simulation tool, requires detailed benchmarking against experiment. In this work, a systematic study is performed on a range of devices (with varying cavity lengths and facet coatings). The amplified spontaneous emission (ASE) spectra are measured as a function of temperature and injection current. From the ASE spectra, the net gain, modal gain, cavity loss and quasi-Fermi level separation are determined.

3.2 The devices

We were provided with a series of edge-emitting $\text{Ga}_{0.613}\text{In}_{0.387}\text{N}_{0.012}\text{As}/\text{GaAs}$ 7nm double quantum well lasers grown [1] by Chalmers University of Technology and processed by Modulight Inc. within the framework of EU project FAST-ACCESS (IST-004772). The quantum wells were separated by 20nm GaAs confinement regions, which were in turn surrounded by 160nm AlGaAs cladding regions. The lasers were processed to have a ridge width of $3.2\mu\text{m}$, formed by $1.3\mu\text{m}$ deep etched

trenches. Uncoated devices had facet reflectivities of 32%, while the coated devices had a front and back facet reflectivities of 30% and 70%, respectively. The devices were of varying lengths ranging from 250 μm to 2000 μm . A list of the devices is shown in table 3.1 and a typical L-I curve from a 300 μm device is plotted in figure 3.1. Increased thermal roll-over and a higher threshold current can be seen as the heat sink temperature is raised.

Length (μm)	Measured Facet (Front/Back/Uncoated)	Device ID	Threshold Current (mA) @25C	Threshold Current (mA) @85C
250	Front	112-15	10.30	15.36
250	Back	112-16	10.99	16.70
300	Front	113-06	12.02	16.57
750	Front	115-18	20.53	29.76
500	Front	122-10	15.20	20.40
500	Uncoated	201-21	18.22	21.92
1000	Uncoated	202-23-203-23	29.21	35.08
2000	Uncoated	207-208-209-210	49.85	51.29

Table 3.1: List of measured device.

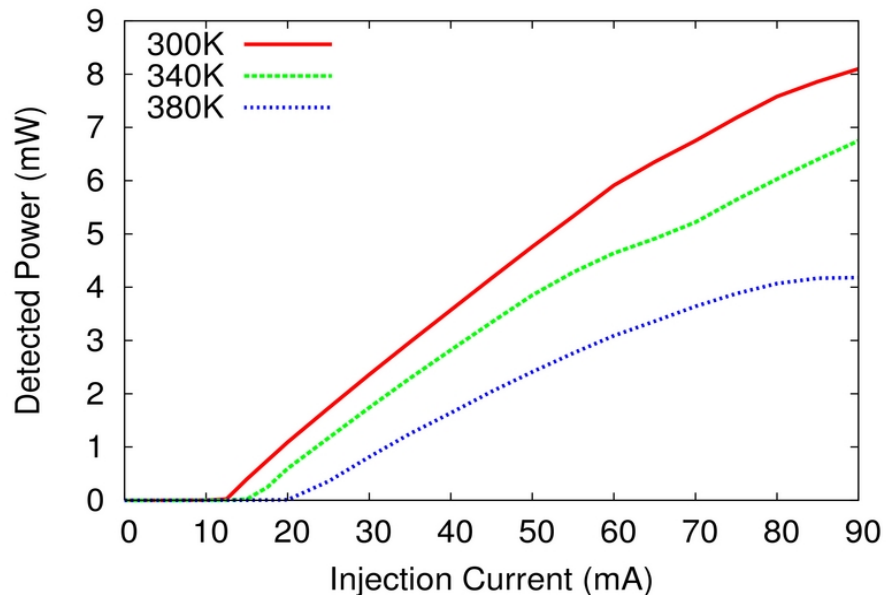


Figure 3.1: Typical power versus current curve of the 300 μ m device

3.3 Direct measurement of gain

The single pass gain of an active medium can be directly measured by illuminating one facet of a laser with a tunable light source, measuring optical the input power and at the other facet measuring the power output [2]. The ratio of output to input power is defined as the single pass gain. For this method to be successful[2] , one requires a widely tunable laser, high quality anti-reflective coatings on the facets of the device and an exact knowledge of the coupling efficiency of the light into the laser and detector. These requirements make the direct measurement of gain very difficult. For this reason, it is common to measure gain using indirect techniques.

3.4 Indirect measurement of gain

Many methods have been described in the literature for the indirect measurement of gain. In this section, a few of the more commonly used methods will be highlighted.

3.4.1 The Hakki-Paoli method

The first method proposed, and subsequently most widely used is the Hakki-Paoli technique [3,4]. The method relies on measuring the ASE spectrum at the front facet below threshold. The modulation depth of the ASE spectrum is used to determine the optical gain [3]. The modulation depth of the ASE spectra is defined as

$$\gamma_i = \frac{P_i + P_{i+1}}{2V_i} \quad , \quad (3.1)$$

where V_i is the amplitude of the i^{th} valley and P_i, P_{i+1} are the amplitudes of the adjacent peaks. Consider a field generated due to spontaneous emission, with propagation constant $k - j\alpha$ where α is the power constant [4]. After the initial field (F_1) has propagated up and down the cavity once, the amplitude is $(R_1 R_2)^{1/2} F_1 e^{-\alpha L}$, where $R_{1,2}$ are the mirror reflectivities and L is the length of the cavity. If the gain of the medium is linear, the total field at the front of the cavity is equal to a superposition of the fields which have propagated throughout the cavity a different number of times. When the fields interfere constructively, the total field at the front facet is given by

$$F_1^+ = F_1 \sum_{n=0}^{\infty} (R_1 R_2)^{n/2} \exp(-n\alpha L) = \frac{F_1}{1 - (R_1 R_2)^{1/2} \exp(-\alpha L)} \quad [4]. \quad (3.2)$$

When the fields interfere destructively, the total field is given by

$$F_1^- = F_1 \sum_{n=0}^{\infty} (R_1 R_2)^n \exp(-2n\alpha L) - F_1 \sum_{n=0}^{\infty} (R_1 R_2)^{n+1/2} \exp(-(2n+1)\alpha L) \quad , \quad (3.3)$$

which yields

$$F_1^- = \frac{F_1}{1 + (R_1 R_2)^{1/2} \exp(-\alpha L)} . \quad (3.4)$$

The fields are related to the powers by

$$F_1^+ = \sqrt{(P^+)} \quad (3.5)$$

$$\text{and } F_1^- = \sqrt{(P^-)} . \quad (3.6)$$

Applying 3.5 and 3.6 [4] one can write

$$-\alpha(\lambda) = \Gamma g - \alpha_i = \frac{1}{L} \left\{ \frac{1}{2} \ln \left(\frac{1}{R_1 R_2} \right) + \ln \left(\frac{\sqrt{(P^+)} - \sqrt{(P^-)}}{\sqrt{(P^+)} + \sqrt{(P^-)}} \right) \right\} , \quad (3.7)$$

which can be rewritten as

$$\Gamma g - \alpha_i = \frac{1}{2L} \ln \left(\frac{1}{R_1 R_2} \right) + \frac{1}{L} \ln \left(\frac{y_i^{1/2} - 1}{y_i^{1/2} + 1} \right) . \quad (3.8)$$

The Hakki-Paoli method relies on only three sampling points - the value at the maxima of the peak and the averaged value of the two minima either side of the peak.

Therefore, this technique is very sensitive to the signal to noise ratio.

This technique is also sensitive to the spectral response of the measurement instrument. A non-ideal instrument response will blur the measured ASE spectra, resulting in the peaks becoming lower and more spread out and the valleys becoming less deep. As the Hakki-Paoli method relies on the peak to the valley ratio, the gain will therefore be underestimated.

3.4.2 Cassidy's improvement on the Hakki-Paoli method

Cassidy proposed [5] a modified method relying on the integrated mode power to the ratio of the minima. This method has two advantages. Firstly, the noise is reduced by \sqrt{N} because the samples are effectively being averaged over the mode. The second advantage comes from the observation that although convolving the ASE spectra by the instrument response alters the heights of the peaks and troughs, it does not alter the overall power in each mode. Thus, Cassidy's method is less sensitive to the instrument response and does not underestimate the gain to the same degree as the H-P method. The steady state spectral output from a laser is given as [5]

$$I^{\pm}(f) = \frac{B(1+R_{\mp}G)(1-R_{\pm})}{(1+RG)^2 - 4RG\sin^2(\theta)}, \quad (3.9)$$

where $-/+$ denote the left and right end of the laser respectively, R_{\pm} are the reflectivities of the mirrors, G is the single pass gain ($G=e^{gL}$), B is the total amount of spontaneous light at frequency f coupled into the lasing mode and $\theta=2\pi Lf/c$. Equation 3.9 gives the minima of the Fabry-Perot at $\theta=0$ and $\theta=\pi$, and integrating over the mode yields [5]

$$I_m^{\pm} = \left(\frac{c}{2l}\right) \frac{B_m(1+R_{\mp}G_m)(1-R_{\pm})}{1-(RG_m)^2}, \quad (3.10)$$

where m denotes the m^{th} mode.

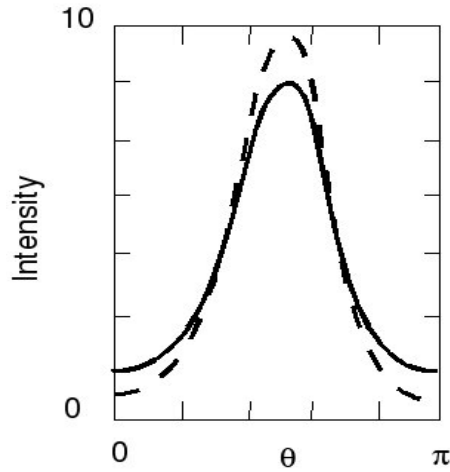


Figure 3.2: A Fabry-Perot mode. The solid line represents the measured mode (i.e. convolved with the system response), while the dotted line represents the actual mode shape [5].

Setting $\theta=0$ in equation 3.9, and taking the ratio of the sum/minima (equation 3.10/equation 3.9) yields

$$p' = \frac{(1 + RG_m)}{(1 - RG_m)} \left(\frac{c}{2l} \right) . \quad (3.11)$$

The variable p is defined as

$$p \equiv \frac{p'}{\Delta f} . \quad (3.12)$$

where,

$$\Delta f = c/2L \quad (3.13)$$

is the free spectral range of the resonator. Rearranging equation 3.11 gives the single pass gain as

$$G_m = \frac{1}{R} \left(\frac{p-1}{p+1} \right) . \quad (3.14)$$

Substituting $G=e^{gL}$ into equation 3.14 and expanding gives

$$g_m = \frac{1}{2L} \ln \left(\frac{1}{R_1 R_2} \right) + \frac{1}{L} \ln \left(\frac{p-1}{p+1} \right) . \quad (3.15)$$

For a discrete spectrum, p may be written as

$$p = \frac{p'}{N \delta \theta} , \quad (3.16)$$

where $\delta \theta$ is the sample width and N is the number of samples within the mode. The ratio of the mode sum to the minima can be redefined as

$$p' = \frac{\sum_{mode} I \delta \theta}{I_{min}} . \quad (3.17)$$

Therefore, p may be expressed as [5]

$$p = \frac{\sum_{mode} I \delta}{I_{min} N} . \quad (3.18)$$

Thus, the gain spectrum may be calculated from equation 3.15.

3.4.3 The least-squares fitting method

Cassidy also recently [2] proposed another method, based on applying a least squares fit to the theoretical Fabry-Perot (FP) spectrum to the measured ASE spectrum. The F-P mode shape is described by the Airy function [2]

$$I(\lambda) = \frac{B(1+RG)(1-R)}{(1-RG)^2 + 4RG \sin^2 \left(\frac{2\pi nL}{\lambda} \right)} , \quad (3.19)$$

where G is the single pass gain, R is the laser facet reflectivity, L is the device length and B is a scaling constant. For fitting, this is expanded around the resonance peak as

$$I(\lambda) = \frac{C}{(1 - P_{RG})^2 + 4 P_{RG} \sin^2 \left(2 \pi n L \left(\frac{1}{\lambda} - \frac{1}{\lambda_0} \right) \right)} \quad (3.20)$$

$$P_{RG}(\lambda) = P_{RG}(\lambda_0) + \beta(\lambda - \lambda_0) \quad (3.21)$$

$$C(\lambda) = C(\lambda_0) + \xi(\lambda - \lambda_0) \quad (3.22)$$

where $P_{RG}(\lambda)$ is the gain reflectivity product and C is a scaling factor. Linear expansions of the gain reflectivity product and C have been used to make the fitting process easier. The Levenberg-Marquardt algorithm is used to fit this function to the experimental data.

For this method to be successful, the spectral response of the system must be known and included in the fitting function, because the measured spectra is far from the ideal FP mode shape. Although the method has been reported to work well below threshold, above threshold the technique performs less well due to deviation (line-width narrowing) of the lasing mode shape from the theoretical one. Another disadvantage of this method is that the fitting algorithm has to be given a good guess for the constants it is expected to find. If a poor guess is provided, it is unlikely to find the correct fit. For every wavelength in a given spectra, a new set of parameters must be given for the initial guess. These parameters vary widely between different wavelengths of a given spectra. This problem is compounded by the change in shape of the mode shape across the spectra. Far away from the gain peak, the mode shape resembles the ideal FP resonance. However, the shape of the lasing modes tends to be far narrower around the gain peak than the ideal FP spectra, which produce false fits.

Thus, the robustness of the method is significantly reduced. In order for the method to be reliable, a very high sample rate and very good signal to noise ratio are required.

3.4.4 True unamplified spontaneous emission

Another set of methods relies on measurement of the true unamplified spontaneous emission (uASE) spectra, which can be used to determine carrier distributions and radiative currents in the QW [6]. If the Fermi-level is known and the assumption of a FD distribution is made, it is possible to extract the gain from the true uASE spectra. The advantage of this technique is that it is less limited by the instrument response and resolution of the measurement equipment, as the fine features of the FP resonances do not have to be resolved. The disadvantage is that in order to measure the true uASE, the detected light leaving the laser must not be absorbed or amplified before detection. This requires the etching of a top contact window in the device. This can be done using ion-beam etching, which is a specialised and expensive processing technique. It should also be noted that the assumption of a single ideal FD distribution far above threshold is questionable, because each subband will have a quasi-independent temperature and Fermi-Level due to the finite intersubband relaxation times.

3.4.5 Segmented contact method

Other methods have also been proposed - most notably the segmented top contact method [6] which requires the top contact of a broad area structure to be etched into several sections. The advantage of this technique is that because no lasing occurs, the

gain does not clamp and the carrier density continues to increase with injection current. Thus, a wide range of gain spectra can be produced by a wide range of carrier densities. The disadvantage is the specialised processing required and the fact that the method can not be performed on an application ready device.

3.4.6 Choice of Cassidy's method

In this work, Cassidy's method was chosen for the following reasons:

1. The devices provided by Chalmers University of Technology and Modulight Inc. were fully processed ridge waveguide lasers without top contact windows. This limited us to measurement of ASE spectra at the front facet.
2. Cassidy's method has been shown to out-perform [2] (in terms of noise and accuracy of gain extracted) all other methods of extracting gain data from the ASE spectra collected at the front facet of a laser diode.

In the next section, the experimental system designed and built as part of this work to measure the ASE spectra is described.

3.5 Description of experimental setup

3.5.1 Overview

A schematic diagram showing the key components of the measurement system is shown in figure 3.3. The laser being measured is mounted on a temperature controlled stage and current is applied via a computer controlled current source. The

ASE is coupled into a single-mode optical fibre connected to an optical spectrum analyser (OSA). The fibre is mounted on a three-axis stage with computer controlled piezo-electric actuators, allowing the collection efficiency to be automatically optimised. It was found necessary to automatically align the fibre before each measurement because of the thermal expansion of the equipment over the range of measurement temperatures. A photograph of the temperature controlled stage and fibre positioner is shown in figure 3.6.

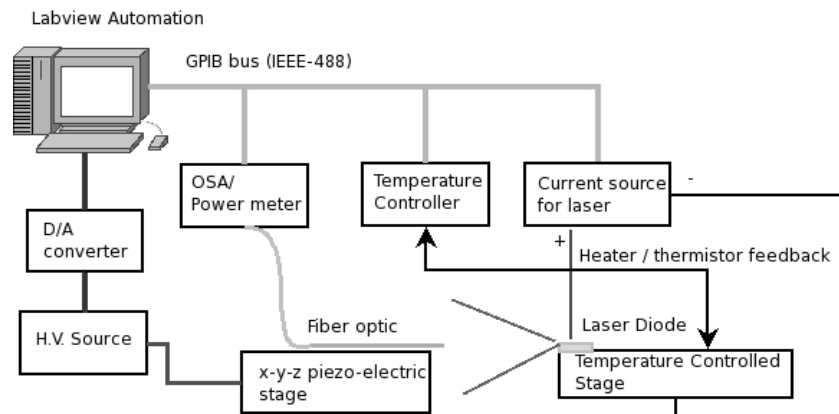


Figure 3.3: The experimental set up.

3.5.2 The devices and sub-mounts

The laser diodes were bonded p-side up to a small copper sub-mount by Modulight Inc. Two lasers bonded p-side up to a sub-mount are shown in figure 3.4. The p-type top contact of the lasers were wire bonded to gold contact pads visible in figure 3.4. Wire bonding the device has two advantages over direct probing. Firstly, the risk of damaging the device during the probing process is eliminated.

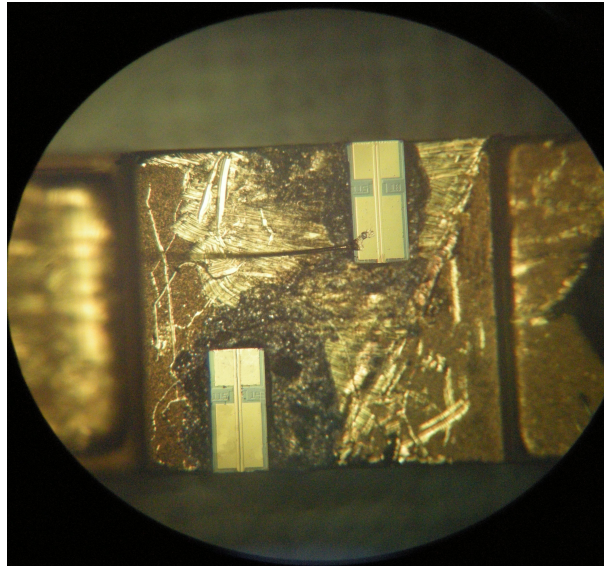


Figure 3.4: Image of the sub-mount and two lasers mounted p-side up. A bonding wire (W) is visible connecting the uppermost laser diode to a contact pad (C) visible in the left of the image.

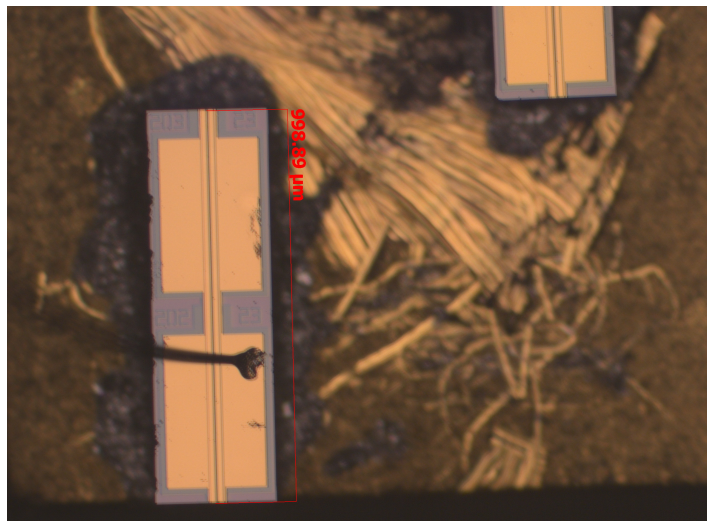


Figure 3.5: An example of a mounted device with the bond wire clearly visible.

Secondly as the temperature of the stage is heated and cooled it expands and

contracts, thus altering the position of the laser relative to the probe, if the laser were directly probed one would run the risk of probe scraping the across the surface of the laser and thus damaging the ridge. A picture of a bonded 1000 μ m device mounted on the heat sink is shown in figure 3.5.

3.5.3 The temperature controlled heat sink

In order to perform measurements at elevated temperatures, a heated stage was required. This consisted of a brass block containing two cartridge heaters and a PT100 thermocouple (complying BS1904 1984, class B). In order to obtain the most accurate temperature reading possible the thermocouple is mounted in a hole drilled directly under the sub-mount. The heaters and the thermistor are connected to a *LakeShore 330 Autotuning Temperature Controller*. Thus, the temperature of the block can be stabilised at any temperature ranging from room temperature to ~390K. The heating block is mounted on a three axis positioner to give maximum maneuverability when aligning the sample. Electrical and thermal isolation between the block and the stage is provided using a 5mm acrylic block. A 0.3mm deep trench the width and length of the sub-mount was milled in the brass block to hold the sub-mount in place during alignment and measurement. A spring steel clip was used to hold the sub-mount firmly against the brass heat sink during the measurement.

3.5.4 Delivery of driving current

The laser driving current was supplied by a *Keithley 220 Programmable current source* via the probe needle (J in figure 3.6), whilst the brass heating block acted as

the negative contact. A probe pin connected to a 3-axes positioner (D in figure 3.6) was used to deliver the current to the gold pad on the sub mount, which was in turn connected to the p-side of the device using a wire bond. A microscope and camera were used to assist with the positioning of the probe pin and the alignment of the fibre. Illumination was provided by a white light source shone through the main lens of the camera. At high illumination power, the light produces a small reverse voltage across the laser, which can be used as a safe way to check the quality of the contact between the probe and the laser. Two *Thurlby 1504 current/volt* meters were used to manually check the current and voltage across the diode.

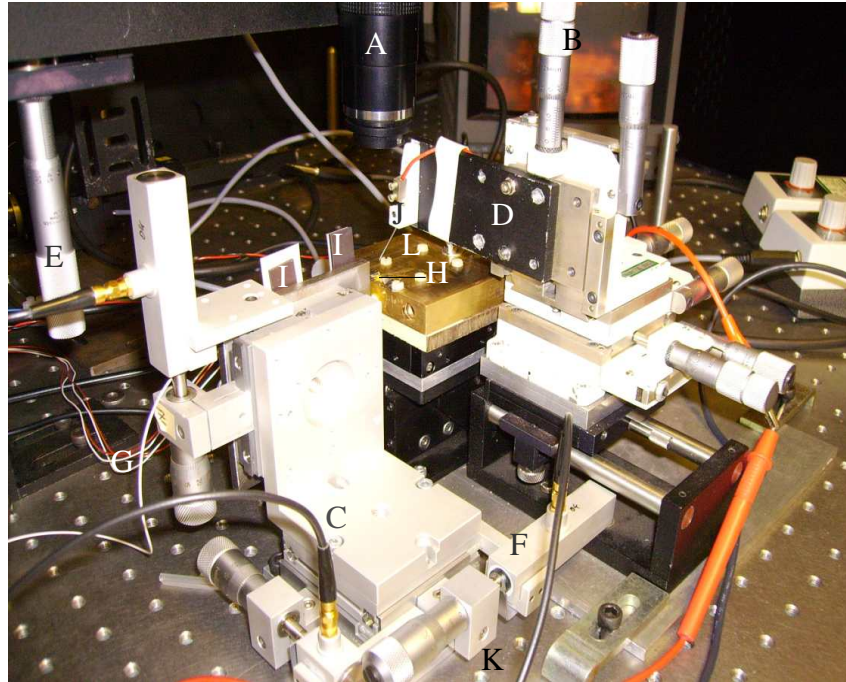


Figure 3.6: The temperature controlled stage and piezoelectric fibre aligner.

- A. Sony CCD video camera positioning camera
- B. CRT display to view the output from the positioning camera
- C. 3-axes piezoelectric controlled stage for alignment of fibre
- D. 3-axes manually controlled stage for probe alignment
- E. Focus control for positioning camera
- F. Piezoelectric stack capable of up to 80µm movement
- G. Single mode fibre optic leading to OSA
- H. Laser diode sub-mount
- I. Magnetic strips holding fibre in place
- J. Probe and probe holder
- K. High voltage (1KV) control lead for piezoelectric stack
- L. Temperature controlled stage

3.5.5 Manual positioning and alignment of the fibre

The fibre was aligned to the front facet of the laser using a *Physik Instrumente 3-axis stage with piezo-electric actuators*. The fibre was held to the stage using a steel plate with a groove milled in it. Flexible magnets were used to clamp the fibre into the groove. The fibre was aligned to the laser using the microscope camera. To further improve the alignment, the laser was run above threshold and a hand held power

meter was used to manually find the position yielding the highest coupling efficiency.

3.5.6 Generation of IV curves

After the automatic alignment was completed, an I-V curve and an L-I curve were made. The L/I curves were taken using the OSA's built-in power meter. Although the optical powers measured were coupled optical power rather than true optical power, this still gives the threshold current and the shape of the LI curve. A *Tektronics TDS 210* digital oscilloscope was used to capture the I-V curves.

3.5.7 Automation

The entire system was automated using LabView, so that it could run 24 hours/day with minimal user input. A program was written to accept a list of currents and temperatures and the software drove the instruments, retrieved the data and saved it to disk. This section describes the operation of the software.

The software initially sends the temperature controller the commands to turn the heating elements on and raise the temperature to the required temperature. The software then monitors the temperature controller until the correct temperature has been achieved and any thermal oscillations have died down. This eliminates the possibility of starting the measurements before the temperature controller's PID control loop converges on the desired temperature. The current source is then directed to supply the first designated current to the laser. The fibre is automatically aligned to the laser by the computer and the OSA instructed to take 20 spectra. The

spectral data is the retrieved from the OSA over the GPIB interface and saved to disk by the computer.

Examples of typical spectra obtained during the course of the measurements are shown in figure 3.7. The shift of peak lasing wavelength as a function of temperature is clear to see. At the end of each measurement, the next current was applied to the laser the fibre realigned and the process started again, when all currents for a set temperature were measured, the computer moved on to the next temperature and the process repeated. Each device took about a week to measure. The system could run for up to 24 hours on its own, however every other temperature increase required manual realignment of the fibre because of the limited movement ($\sim 80\mu\text{m}$) of the piezoelectric stacks.

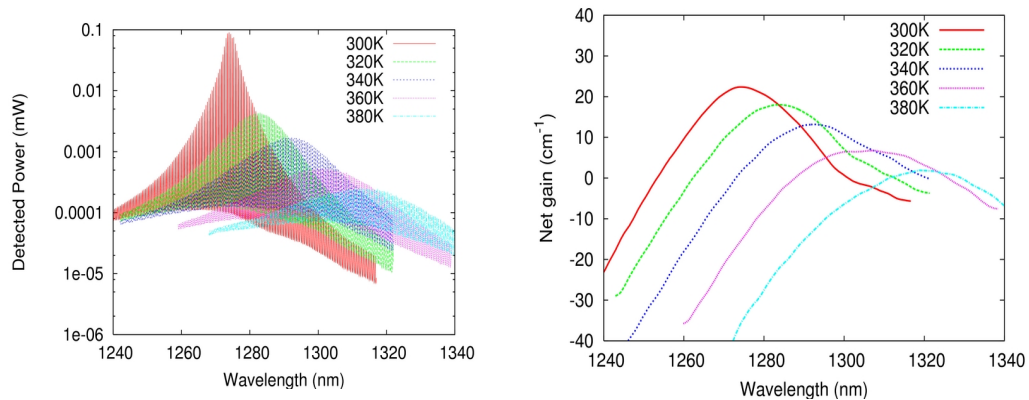


Figure 3.7: Typical spectra measured by the experimental system (left) and gain spectra extracted from the spectra taken at 20mA (right).

3.5.8 Automatic positioning and alignment of the fibre

The brass heating block expands when the temperature is varied. The sub-

mount/laser assembly also expands very slightly when large currents are applied to the devices. (This is a particular problem with long cavity devices.) Thus, in order to achieve the maximum coupling efficiency and the best SNR possible, the fibre must be realigned between measurements. To do this, the *Anritsu MS9710C Optical Spectrum Analyser* is placed in its power meter mode. A PC running LabView 8.0 is used to read the OSA's power reading and a *Physik Instrumente P-263 High voltage power supply* was used to drive the piezostacks on the stage holding the fibre. The power supply was connected to the computer via a *National Instruments A/D* board. In this way, a feedback loop is established whereby the fibre can be automatically realigned one axis at a time. The automatic alignment produced significantly better alignment than could be achieved by hand. Once the alignment was finished. The OSA was set back to measurement mode, so that spectra could be obtained.

3.6 Measurements

Measurements were performed for each device at heat sink temperatures of 300K, 320K, 340K, 360K and 380K. Approximately 20 bias currents per temperature were measured in 1mA steps, from far below threshold to slightly above. Spectra were measured over 80nm using 5000 sample points, the OSA had a resolution (FWHM) of 0.05nm and an optical reception sensitivity of -90 dBm.

3.7 Post processing - Peak and trough finding

Before Cassidy's method can be applied, a robust method must be found to extract the positions of the troughs from the spectral data. These were found by determining the

points within the spectra at which the gradient of the energy with respect to wavelength changes from negative to positive. For the Hakki-Paoli method, the position of the peaks must also be determined. This is done by finding the points at which the gradient of changes from positive to negative. This algorithm and Cassidy's method were implemented in an external C++ program used to post-process the data. The Cassidy and the Hakki-Paoli methods were both implemented in the post processing software.

3.8 Calculation of modal gain and loss

Both Cassidy's method and the Hakki-Paoli method calculate the net modal gain of the active region,

$$g_{net} = g_m - \alpha \quad , \quad (3.23)$$

where the net modal gain is defined as the modal gain minus the internal loss. The internal loss is a very useful parameter to know for the calibration of a device simulator. It can be calculated from the modal gain spectrum if one recognises that at the low energy side of the band edge, the theoretical gain g_m tends to zero, because there are no carriers below the band edge. (Any gain measured in this region is due to the finite lifetime of the carrier scattering events, i.e. broadening processes.) Thus, the difference between the low energy tail of the gain spectrum and the 0 cm^{-1} net modal gain line, by equation 3.23 gives the cavity loss α . This is depicted in figure 3.8.

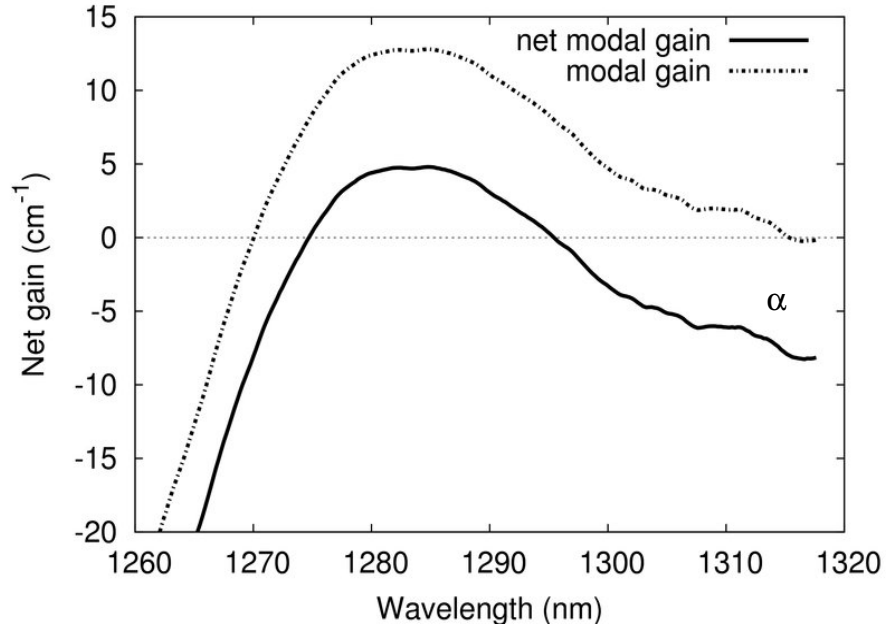


Figure 3.8: An example of a net modal gain curve shifted up by the cavity loss to align the gain tail with 0cm^{-1} resulting in a modal gain curve.

3.9.1 Calculation of quasi-Fermi level separation

Once the net modal gain curve has been shifted up by the internal loss α to produce the modal gain curve, the intersection of the gain curve and 0 cm^{-1} gain line at the high energy side the spectra gives the separation of the quasi-Fermi levels [7] i.e.

$$F_2 - F_1 \geq E_2 - E_1 \quad (3.24)$$

must be fulfilled for the probability of a downward transition to be greater than that of an upward transition where F_2 , F_1 are the quasi-Fermi levels and E_2 and E_1 are the energies of the electrons and holes. Thus, the internal loss and the quasi-Fermi level separation can be obtained.

3.9.2 Other methods for the calculation of the quasi-Fermi level separation

Ideally the method described above is enough for Fermi level extraction. However, the drawback to this method is that the low energy tail of the gain spectra is very weak and usually has a very low signal to noise ratio (SNR). There are other methods which directly extract the quasi-Fermi level separation. For example, the author in [8] suggested that when the gain curves for the TE and TM modes intersect the material gain is zero. Shtengel [9] proposed measuring the junction current of a diode modulated externally using a probe laser, the small changes in junction voltage are monitored as the tunable probe laser searches for the transparency point. The drawback of this method is that a very accurate tunable laser [10] must be used and measuring the tiny changes in junction voltage is also problematic [10]. A method which can extract the quasi-Fermi level separation from the modulated ASE spectra would therefore be very useful. Such a method was recently presented by Lin-Zhang [11]. Using Einstein's relations for optical transitions, a relationship between the stimulated and spontaneous emission rates may be established [12-14]

$$C_{SPE} \cdot g(E) = \frac{\pi^2 \hbar^3 c^2}{(E)^2 \cdot n_{eff}^2} \left[1 - \exp\left(\frac{E - \Delta E_f}{kT}\right) \right] I_{SPE}(E, \Delta E_f) \quad , \quad (3.25)$$

where $g(E)$ is the material gain, E is the photon energy, $I_{SPE}(E, E_f)$ is the spontaneous emission (SPE) detected in arbitrary units, C_{SPE} is a scaling factor between the real SPE and the detected SPE and n_{eff} is the effective index. By differentiating 3.25 with respect to E , at the energy corresponding to the gain peak, E_{gp} the differential of the gain with respect to energy is zero. Therefore, the following relationship may be established between the quasi-Fermi level separation and the gain peak [12]

$$\Delta E_f = E_{gp} + kT \ln \left(1 + \frac{1}{R'} \right) \quad (3.26)$$

where,

$$R' = kT \left(\frac{1}{I_{spe}} \frac{dI_{spe}}{dE} - \frac{2}{E} \right)_{E=E_{gp}} \quad (3.27)$$

The signal pass ASE can be related to the spontaneous emission by

$$C_{ASE} \cdot I_{ASE}(hf, \Delta E_f) = \frac{1}{g_{net}} [\exp(g_{net} L) - 1] I_{spe}(E, \Delta E_f) \equiv I_{ASE}(E, \Delta E_f) \quad (3.28)$$

By differentiating equation 3.28 with respect to energy at the gain peak, the following relation can be derived

$$S' = \frac{1}{I_{spe}} \cdot \frac{dI_{spe}}{dE} \Big|_{E=E_{gp}} = \frac{1}{I_{ase}} \cdot \frac{dI_{ase}}{dE} \Big|_{E=E_{gp}} \quad (3.29)$$

The single pass ASE can be extracted from the spectra using

$$I_{ASE} = P^+ P^- \left([\sqrt{P^+} + \sqrt{P^-}] / 2 \right)^2 \quad (3.30)$$

Therefore, R' can be evaluated and the quasi-Fermi level separation extracted. With a simulated ASE spectra convolved with an instrument response function, the quasi-Fermi level separation can be found to within 0.1meV, which is acceptable. However, due to the noise present in measured spectra, the method becomes more unreliable for real data. The first problem is that the gain peak must be found very accurately and because the gain peak can be relatively flat, any noise can shift the peak. A second problem is that because the single pass ASE (SP-ASE) is extracted using a formula relying on the modulation depth of the ASE spectrum, it is prone to error introduced by the instrument response and numerical noise. Apart from this, it

relies, on the gradient of the ASE with respect to energy, so any small amount of noise introduced in the ASE will produce large errors. Various fitting techniques were used in an attempt to extract the SP-ASE gradient correctly, but proved unsuccessful. Although this method would appear to be attractive, the experimental data must be *very* clean and of *very* high resolution. After much work, the most reliable and robust method for extraction of the quasi-Fermi level separation turned out to be that described in the previous section 3.8.

3.10 Extraction of effective group index and alpha factor

3.10.1 Calculation of effective group index

The effective group index can be extracted from the ASE spectra by examining the mode spacing of the cavity. The effective group index is defined as

$$n_g = n_{eff} + f \frac{\partial n_{eff}}{\partial f} , \quad (3.31)$$

where n_{eff} is the effective index and f is frequency. For the device to reach lasing threshold, the gain must be large enough for the optical field to reproduce itself every round trip [15] i.e. β must satisfy

$$\sqrt{R_1 R_2} \exp(2i \beta L) = 1 . \quad (3.32)$$

At threshold, if R_1 and R_2 are the power reflectivities of the mirrors and β is the propagation constant

$$\beta = n k_0 + i \alpha / 2 . \quad (3.33)$$

Substituting 3.33 in 3.32 and equating the real and imaginary parts results in the unity round trip gain condition

$$\sqrt{R_1 R_2} \exp(-\alpha L) = 1 \quad (3.34)$$

and the round trip phase matching condition

$$\sin(2 n k_0 L) = 0 \quad (3.35)$$

For 3.35 to be satisfied, the relation

$$2 n k_0 L = 2 m \pi \quad (3.36)$$

must be fulfilled. Equation 3.36 can then be used to determine the mode spacing of the cavity, by considering the mode m and the mode $m+1$,

$$f_0 n_0 = \frac{m c}{2 L} \quad (3.37)$$

$$f_1 n_1 = (m+1) \frac{c}{2 L} \quad (3.38)$$

Subtracting 3.37 for m and $m+1$ results in

$$\Delta(f n) = \frac{c}{2 L} \quad (3.39)$$

where the refractive index is wavelength dependent. Using the chain rule, the change in refractive index and frequency can be written as

$$\Delta(n f) = n \Delta f + f \Delta n \quad (3.40)$$

Using equation 3.40, equation 3.39 can be rewritten as

$$\Delta f = \frac{c}{2 n_g L} \quad (3.41)$$

Using the standard formula

$$\Delta f = c \frac{\Delta \lambda_m}{\lambda_1 \lambda_2} \quad (3.42)$$

where $\Delta \lambda = \lambda_2 - \lambda_1$, in equation 3.41, an expression for the effective group index can be

written in terms of wavelength as

$$n_g = \frac{\lambda_1 \lambda_2}{2 L \Delta \lambda_m} . \quad (3.43)$$

Although the above derivation may appear trivial, in the literature it is common to confuse effective phase index and effective *group* index. This mistake is made by neglecting the wavelength dependence of the effective index in equation 3.40 and is therefore a point worth highlighting.

3.10.2 Extraction of the peak position

In order to implement equation 3.43, the exact position of each peak must be known. Because the resolution of the OSA is not high enough to resolve the position of the peaks exactly, a weighted average over the mode was used to improve the peak position estimation. This weighted average can be calculated as

$$\lambda_{pos} = \frac{\sum_{\lambda_{min1}}^{\lambda_{min2}} \lambda P^2(\lambda)}{\sum_{\lambda_{min1}}^{\lambda_{min2}} P^2(\lambda)} \quad (3.44)$$

where λ is the wavelength and $P(\lambda)$ is the measured power. The sum is performed between the two minima. The power term was found to enhance the peak relative to the trough thus making weighted mean more accurate. This method was found more robust for the large amounts of data than the traditional approach of fitting a parabola to each peak and extracting the peak position from the maximum.

3.10.3 Extraction of shift of effective index (Δn_{eff})

Although it is not possible to calculate the absolute value of the effective index from the ASE spectra, it is possible to calculate a good approximation to the change of the effective index as the bias current is changed. The spectral position of a mode at current I_0 can be written as,

$$f_0 n_0 = \frac{mc}{2L} \quad (3.45)$$

and at current I_1 the position can be written as

$$f_1 n_1 = \frac{mc}{2L} \quad (3.46)$$

Subtracting equation 3.45 from equation 3.46, one can write

$$\Delta(f_0 n_0) = 0 \quad (3.47)$$

Expanding equation 3.47 using the chain rule results in

$$\Delta(n f) = n \Delta f + f \Delta n = 0 \quad (3.48)$$

which can be rearranged to give,

$$\Delta n = -\frac{n \Delta f}{f} \quad (3.49)$$

Writing equation 3.49 in terms of lambda gives

$$\Delta n = -n \left(\frac{c}{\lambda_1} - \frac{c}{\lambda_0} \right) \frac{\lambda_0}{c} \quad (3.50)$$

Therefore

$$\Delta n = -n \left(\frac{\lambda_1 - \lambda_2}{\lambda_1} \right) = n \frac{\Delta \lambda_s}{\lambda_1} . \quad (3.51)$$

Substituting equation 3.43 into equation 3.51, results in

$$\Delta n_{eff} = \frac{\Delta \lambda_s \lambda}{2 L \Delta \lambda_m} , \quad (3.52)$$

which may be used to calculate the shift in effective index with increased bias current. Again the derivation may seem trivial. *However*, one assumption was made in the last step and this is that n_g (calculated from equation 3.43) has been substituted for n - this is commonly not appreciated in the literature. The assumption was first introduced by Turley in 1979 [16] with no mention of the assumption being made. As mentioned before ,

$$n \neq n_g . \quad (3.53)$$

The effective group index is usually around 10% larger than the group index. Therefore, a 10% overestimation of the effective index shift is introduced by using this expression. Despite this overestimation, it remains the only piratical way to extract the effective index shift in the cavity using the change in wavelength of resonant modes.

3.10.4 The Kramer's-Kronig relations and the extraction of the alpha factor

The Kramers's-Kronig relations inextricably link the real and imaginary parts of any physically reasonable spectra. This is particularly important in optoelectronic

devices, where a change in the gain is linked to a change in the refractive index. Thus, when a device is directly modulated altering the carrier injection rate and thus the gain, the refractive index is unavoidably changed. A change in the refractive index alters the effective length of the cavity. Since the resonant frequency of the cavity depends upon the optical length, the modulation produces changes in the lasing frequency. This effect is named dynamic chirp. The linewidth enhancement factor (LWEF) α , often called the alpha or Henry factor, is often used as a measure of chirp and the level of interaction between the gain and the effective index shift. It is defined as

$$\alpha = -2k \frac{dn_{eff} / dn}{dg_{eff} / dn} = -2k \frac{\Delta n_{eff}}{\Delta g_{eff}}, \quad (3.54)$$

where n_{eff} , n , g_{eff} and k , are the effective index, carrier density, modal gain and free space wave-vector, respectively. The magnitude of the alpha factor is a measure of how dependent the effective index is upon the gain and as such is a measure of chirp. The alpha factor is particularly important when modulating laser diodes – the larger the alpha factor, the larger the lasing frequency shift when directly modulated. The alpha factor is however a linear concept applicable only for small-signal modulation conditions. A table of alpha factors for various devices is shown in table 3.2.

If the gain spectrum is known over a wide enough wavelength range and the integrand of the Kramers's-Kronig relationship approaches zero at the maximum measured energy, it is possible to directly extract the effective index and thus the alpha factor.

Alpha factor	λ (nm)	Year of publication	Method	Number of QWs	Structure	Structure	Ref
3.5	1310	1987	FP	4	EE-QW	InGaAsP/InP	[32]
1.5-5.0	1070	1989	FP	1	EE-QW	InGaAs-GaAs	[33]
1.0-2.0	1300	1990	FP	3	EE-QW	InGaAsP/InP	[34]
2.6	1550	1990	FP	3	EE-QW	InGaAs/InP	[35]
1.5	1500	1991	FP	4	EE-QW	InGaAs/InP	[36]
1.5	1500	1991	FP	4	EE-QW	InGaAs/InP	[37]
0.85	1500	2007	Theoretical	1	EE-QW	InGaAs-InP	[38]

Table 3.2: Alpha factors from the literature.

3.10.5 Thermal and electrical shifts in effective index

In figure 3.9, the shift of one of the FP modes is plotted as a function of injection current. Below threshold, the peak blue shifts as the refractive index decreases due to the increasing gain. Above threshold, the gain is clamped, so that no further decrease in refractive index takes place. At this point, thermal effects start to dominate [16] and the FP peak red shifts. Although carrier induced effects dominate the effective index change below threshold, thermal effects also play a role. If one wishes to obtain the magnitude of the carrier induced blue shift below threshold (for example, for calculating the alpha factor), then thermally induced red shift must be subtracted from the measured shift in the FP peak. It is common to do this by assuming the same thermally-induced red shift ($\Delta\lambda/\Delta I$) above threshold and below threshold. [17]

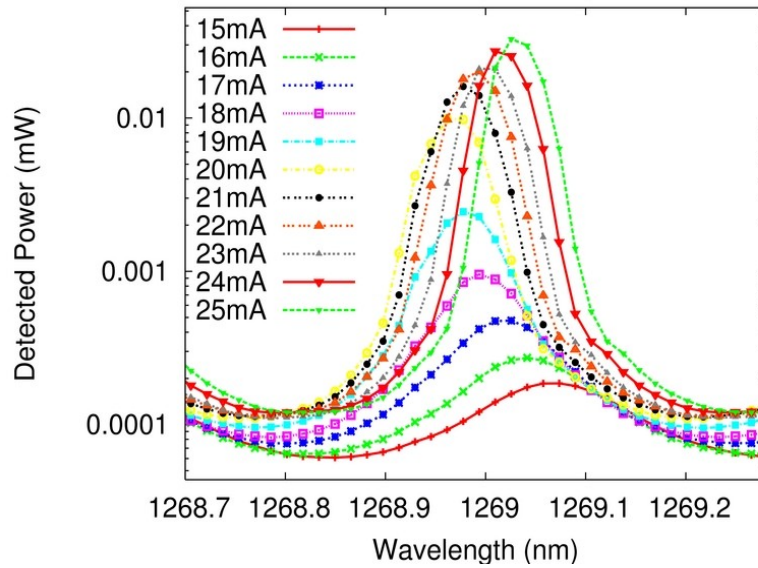


Figure 3.9: Shift of a FP resonance close to lasing peak at 380K.

3.11 Errors in the measured signal

3.11.1.1 Verification of the waveguide integrity

The use of Cassidy's method requires high-quality ASE spectra from defect free devices. If the devices degrade during the course of the measurements due to either defect formation or indeed due to physical damage, sub-cavities could have been formed within the device [18]. The formation of such sub-cavities perturbs the ASE spectra and invalidates the use of both Cassidy's method and the Hakki-Paoli technique. To ensure the integrity of the lasers and thus of the extracted gain spectra, a method employed by Klehr *et al.* [18] and later improved upon by Bream *et al.* [19] was used to check for the formation of defects before and after each measurement. In this method, the Fourier-transform of the spectrum of a laser is taken. Then, the expression

$$L = \frac{\lambda^2}{2n_g \Delta \lambda} \quad (3.55)$$

is used to rescale the Fourier transform of the spectra in terms of the cavity length. The Fourier transform has a large peak corresponding to the DC frequency components of the spectra and another peak corresponding to the length of the cavity (see figure 3.10). For a defect-free cavity, only one resonance should occur at a position equal to the cavity length. Resonances that occur at other cavity positions indicate perturbations / defects within the cavity. All of the devices supplied to us were checked and found to be undamaged. This check was also performed on all spectra before the gain was extracted to make sure no damage had occurred during the measurements.

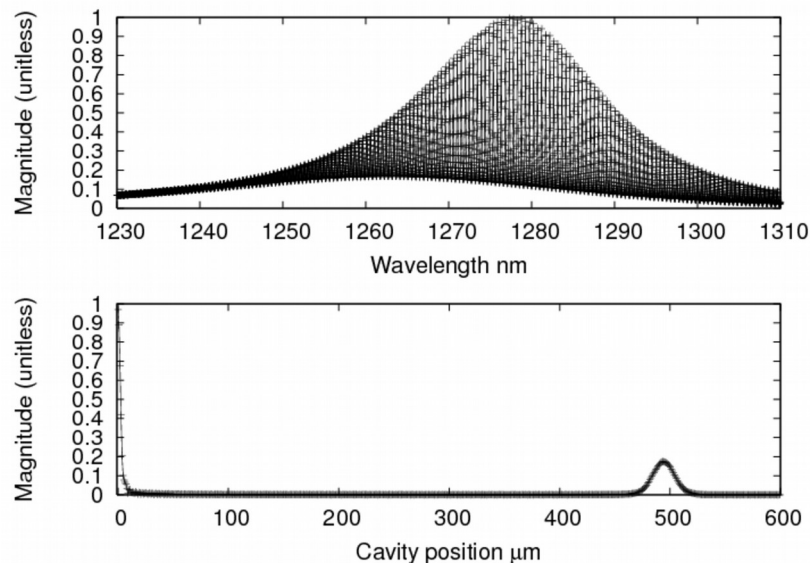


Figure 3.10: Fourier transform of the below threshold spectra for a 500 μm cavity.

3.11.1.2 A method for refractive index extraction

If equation 3.55 is rearranged in terms of the refractive index, the Fourier transform can be rescaled in terms of the refractive index

$$n_g = \frac{\lambda^2}{2L\Delta\lambda} . \quad (3.56)$$

It was hoped that by examining the position of this peak, the effective index could be extracted from the ASE spectra. However, the simulation results showed that the effective index could only be extracted to within ± 0.05 and that the peak shifted to longer wavelengths for higher carrier densities. The inaccuracy in the extraction of the group index was found to be due to the gain spectra shifting as the carrier density was changed. This resulted in the Fourier transform, picking out slightly different dominant resonant frequencies for each carrier density. The method is good enough for determining the position of defects within a cavity, but not good enough to determine the exact group index.

3.11.2 Deconvolution and estimation of system response

The FP modes of an ASE spectrum are often comparable in width to the instrument response of a good quality OSA. Therefore, when measuring the ASE spectra, even with an instrument with a very narrow spectral response [20], the spectral response of the OSA must be considered. It was therefore necessary to determine how much the ASE spectra were affected by the spectral response of the OSA and thus determine the accuracy of the extracted gain spectra. When any signal is measured, the acquired measurement is always the signal $s(f)$ which one wishes to measure convolved with

the spectral response $r(f)$ of the measurement system. In this set-up, the measured signal is the modulated ASE from the laser convolved with the response of the fibre $b(f)$, then convolved with the response of the OSA. Thus, the measured spectra $m(f)$ can be written as

$$m(f) = r(f) * s(f) * b(f) \quad . \quad (3.57)$$

To extract the signal $s(f)$, the exact response of the measurement system must be known, in this case $r(f) * b(f)$. To obtain this function an optical source with a known spectra must be used, for example a benchtop tunable laser. Using the measurement system, a known optical source is measured and the result deconvolved with known spectra of the source. The result is the system response. i.e.

$$s(f) = m(f) / (r(f) * b(f)) \quad . \quad (3.58)$$

Unfortunately, no stable source was available at the desired wavelength and it was not possible to obtain the exact response of the OSA from the manufacturer. A further problem with deconvolution is that the data must be *very* clean or the noise is simply sharpened above the level of the signal [21]. Because our signal was very weak, deconvolution often produced poor results. The best solution is to use Cassidy's method because of its insensitivity to the system response, whilst estimating the error the system response introduces into the measurements. The error was estimated by simulating the ASE and convolving it with an *approximation* to the system response. The length of the fibre was very short (under half a meter) and was specifically designed to be capable of transmission over tens of kilometers; $b(f)$ is therefore

assumed to be a constant. The OSA's data sheet gives the following information about its spectral response (table 3.3).

Full width half maxima	0.07nm
Dynamic range @0.2nm from peak	42dB
Dynamic range @0.4nm from peak	58dB
Dynamic range @1nm from peak	62dB

Table 3.3: Information available from the manufacturer about the system response.

The spectral response of the OSA is very sharp near the center frequency (i.e. Gaussian). However, further away from the FWHM, a slower roll off is seen (i.e. Lorentzian). Therefore, the sharp peak was approximated with a Gaussian. This was added to a Lorentzian to simulate the slow roll off after the sharp peak. At 10nm from the peak, the system response was assumed to be 0. The function is given in equation 3.59, where the constants were determined by fitting.

$$g(\lambda) = \begin{cases} \text{when } \lambda < 10\text{nm} & C \left(\exp\left(\frac{-\lambda^2}{2c^2}\right) + \frac{y}{4000\pi\left(|\lambda|^3 + \frac{y^2}{4}\right)} \right) \\ \text{else} & 0 \end{cases} \quad (3.59)$$

where

$$y = 0.008 \quad (3.60)$$

and C is a normalisation constant

$$C = \frac{1}{\int_{-\infty}^{\infty} g(\lambda) d\lambda} \cdot \quad (3.61)$$

Equation 3.59 has been plotted as the dotted line in figure 3.11. The point at which the Gaussian stops dominating the function is clear to see at 0.15nm. The points from the OSA data sheet have also been plotted on the graph. In order to verify the correctness of this assumption, a Fujitsu FLD3F11CX 1.310nm MQW-DFB laser with a very narrow line width was taken and measured with the OSA. The linewidth of a DFB laser is typically 25MHz which is far below the resolution of the OSA. This can therefore be approximated as a delta function, so that the measurement results in an estimation of the spectral response of the OSA. As can be seen from the figure 3.11, the measured response of the OSA and the response given in the manual are in good agreement. Unfortunately, the DFB laser has side lobes, one of which can be seen in the figure. This prevents the measured response being used for deconvolution.

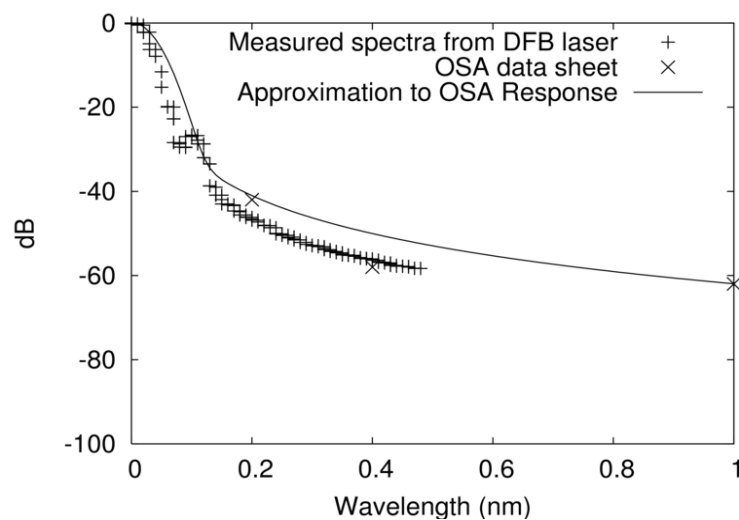


Figure 3.11: Spectral response of the OSA.

3.11.3 Estimation of error in the measured data

In order to estimate how the system response impacts the measurement of gain, our in-house gain simulation tool was used to calculate the theoretical spontaneous and

stimulated emission rates for the devices. The ASE spectrum was calculated using the stimulated and spontaneous emission rates. Our model uses a 4x4 $k \cdot p$ band model to calculate the valence band structure and a band anti-crossing model [22] to calculate the conduction band structure. Fermi-Dirac statistics and Fermi's golden rule [23] were used to calculate the optical emission rates. The ASE spectra were then calculated for different carrier densities, and cavity lengths using a Fox-Li iteration scheme. The calculated spectra were then convolved with a function approximating the measured instrument response. (see figure 3.12) The impact of the convolution can be best seen in figure 3.13, where the peaks are lower and the troughs have been raised.

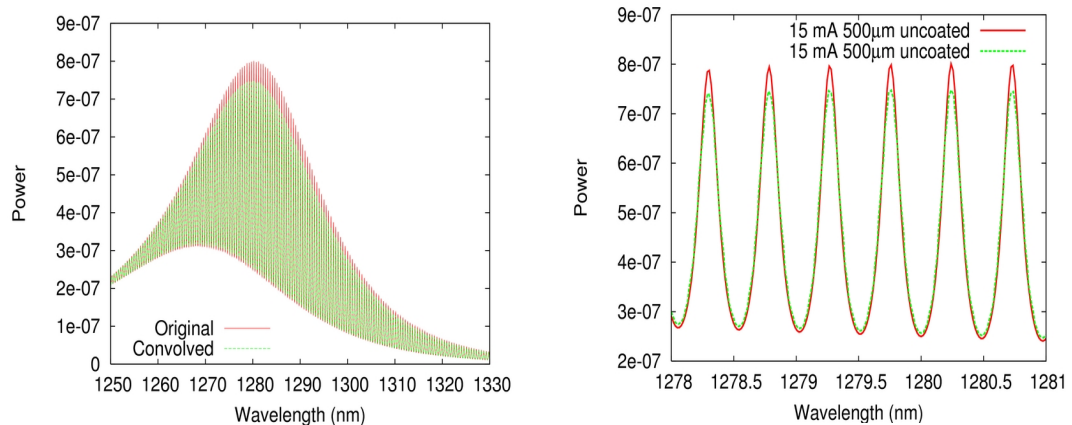


Figure 3.12: Calculated ASE spectra - both the original and convolved spectra are shown. *Figure 3.13: Zoomed in section of figure 3.12.*

Gain spectra were then extracted from the convolved ASE spectra. The difference between the gain spectra calculated from the convolved and unconvolved ASE spectra

were then compared, giving an estimate of the error introduced into the measurements by the spectral response of the OSA. Figure 3.14 shows two such gain spectra, one original spectrum, and one spectrum extracted after convolution.

A series of devices of varying lengths at different carrier densities were studied. The results of the calculations are shown in table 3.4. The simulated carrier densities are given in the caption to each table. The first column in the table gives the simulated device length. The second column gives the peak modal gain calculated before convolution. The column entitled Cassidy and HP, are the values of *modal gain* extracted from the simulated ASE spectra *after* convolution with the system response. The next column, gives the value of simulated *net gain* before convolution. Again, the columns Cassidy and HP give the extracted value of net-gain extracted from the convolved ASE spectra. For the measurements presented here, the maximum error is 1.0cm^{-1} for the net gain and 1.6cm^{-1} for the modal gain.

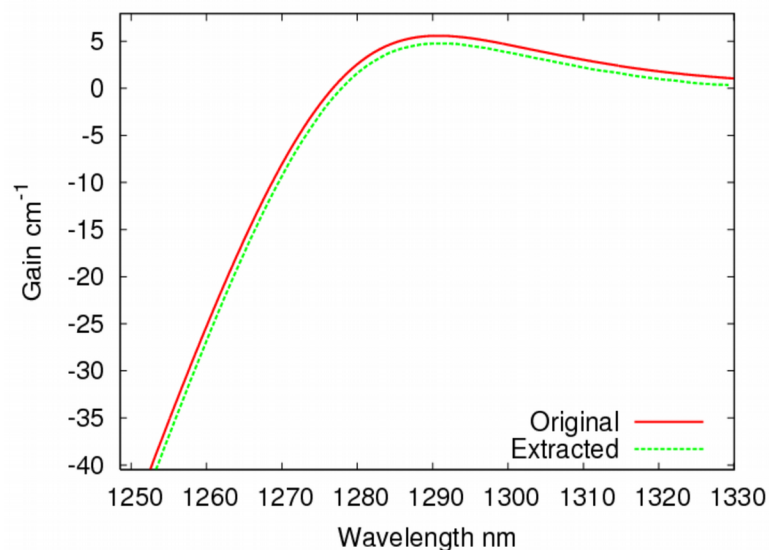


Figure 3.14: Gain used to generate ASE spectra and gain extracted from ASE spectra after convolution.

It can be seen from table 3.4 that the modal-gain can be found far more accurately than the net gain. This is because the effect of convolution on the ASE spectra is to reduce the height of the peaks and fill in the troughs. The H-P, and to a lesser extent Cassidy's, method then underestimate the gain. This results in the whole spectra being *shifted* downwards, but with little change in its shape. Thus, by shifting the spectra up to zero to find the modal gain, the error introduced is reduced. However, this error will reappear in the estimation of the internal loss. Due to the superior performance of Cassidy's method, only this method will be used in the rest of this work to extract the gain spectra from the modulated ASE spectra.

	modal-gain			net-gain			
Length	True value (cm ⁻¹)	Cassidy (cm ⁻¹)	H-P (cm ⁻¹)	True Value (cm ⁻¹)	Cassidy (cm ⁻¹)	H-P (cm ⁻¹)	$\Delta\lambda$ (nm)
250 μ m	9.12	8.75	8.69	4.12	3.25	3.15	0.03
500 μ m	9.12	8.95	8.50	4.12	2.86	2.36	0.03
1000 μ m	9.12	8.15	7.38	4.12	2.29	1.26	0.016

Table 3.4a: At a carrier density of $1.4 \times 10^{24} \text{m}^{-3}$.

	modal-gain			net-gain			
Length	True value (cm ⁻¹)	Cassidy (cm ⁻¹)	H-P (cm ⁻¹)	True Value (cm ⁻¹)	Cassidy (cm ⁻¹)	H-P (cm ⁻¹)	$\Delta\lambda$ (nm)
250 μ m	13.43	13.06	12.89	8.43	7.59	7.38	0.03
500 μ m	13.43	13.41	12.63	8.43	7.39	6.56	0.03
1000 μ m	13.43	12.88	11.60	8.43	7.44	5.85	0.016

Table 3.4b: At a carrier density of $1.5 \times 10^{24} \text{m}^{-3}$.

	modal-gain			net-gain			
Length	True value (cm ⁻¹)	Cassidy (cm ⁻¹)	H-P (cm ⁻¹)	True Value (cm ⁻¹)	Cassidy (cm ⁻¹)	H-P (cm ⁻¹)	$\Delta\lambda$ (nm)
250 μ m	18.23	17.94	17.56	13.23	12.51	12.09	0.03
500 μ m	18.23	18.42	17.23	13.23	12.49	11.24	0.03
1000 μ m	A.T.	A.T.	A.T.	A.T.	A.T.	A.T.	0.016

Table 3.4c: At a carrier density of $1.6 \times 10^{24} \text{m}^{-3}$.

	modal-gain			net-gain			
Length	True value (cm ⁻¹)	Cassidy (cm ⁻¹)	H-P (cm ⁻¹)	True Value (cm ⁻¹)	Cassidy (cm ⁻¹)	H-P (cm ⁻¹)	$\Delta\lambda$ (nm)
250 μ m	23.32	23.07	22.48	18.32	17.69	17.05	0.03
500 μ m	23.32	23.84	22.29	18.32	18.01	16.39	0.03
1000 μ m	A.T.	A.T.	A.T.	A.T.	A.T.	A.T.	0.016

Table 3.4d: At a carrier density of $1.7 \times 10^{24} \text{m}^{-3}$.

A.T. = Above threshold, $\Delta\lambda$ =simulated spectral resolution of the OSA.

3.12 Experimental results and analysis

3.12.1 Gain measurement

The experimental net gain spectra of the uncoated 500 μ m device are shown in figure 3.15 for all measured temperatures and at a constant current of 20mA.

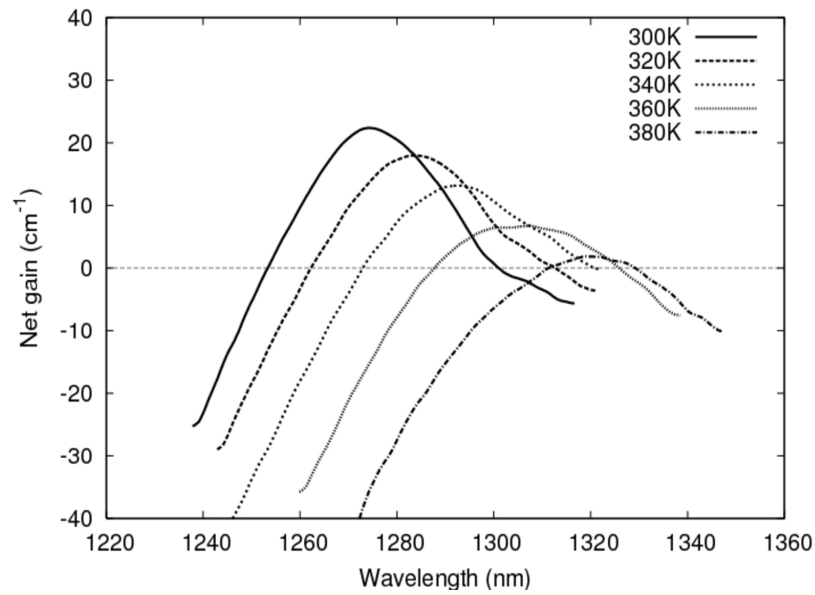


Figure 3.15: Net gain spectra as a function of temperature for the uncoated 500 μ m device at a constant current of 20mA.

The changes in the gain curves in figure 3.15 are due only to thermally induced effects. As the temperature is increased, the value of the net gain reduces at a rate of 0.26cm⁻¹/K, which is comparable to the typical values of 0.30cm⁻¹/K obtained for InP-based devices [24]. The gain spectra broaden and red shift at a rate of 0.56nm/K, which is also comparable to the 0.3-0.5nm/K commonly obtained from more traditional InP-based devices [24]. Examination of the gain spectra for all the devices measured allowed the internal loss to be determined as described previously. A value of 8.0 \pm 1.6cm⁻¹ was found for the devices investigated, which is again comparable to that obtained for many InP-based devices.

The measured internal losses were found to be independent of the carrier density/temperature, indicating inter-valence band absorption in these devices is small

compared to InP-based devices. This may be due to the larger separation between the heavy-hole and split-off valance bands.

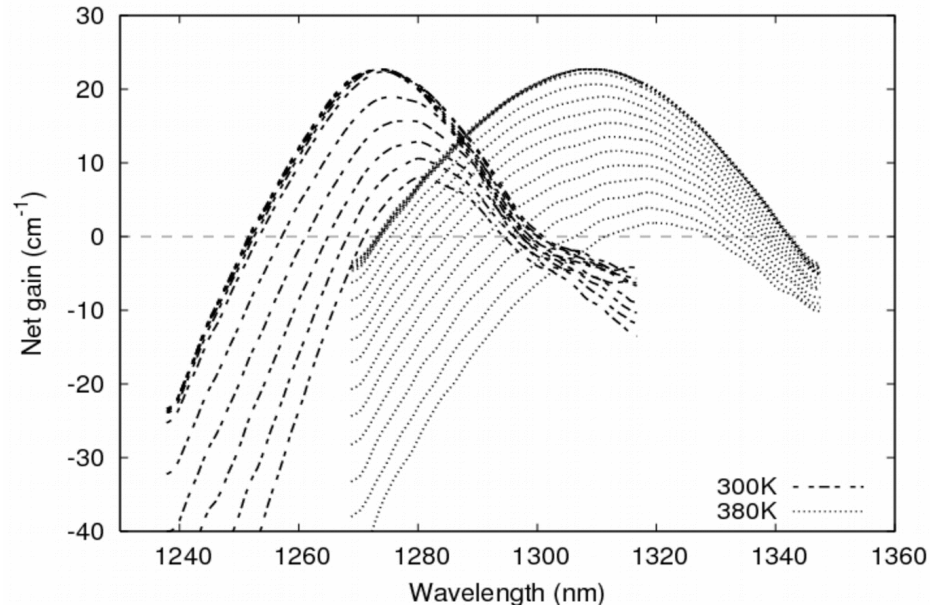


Figure 3.16: Gain spectra for the 500 μ m device at 300K and 380K. At 300K, the lowest curve was produced with an injection current of 15mA. At 380K, the lowest curve was produced with an injection current of 20mA. The spectra are plotted for currents increasing in 1mA steps.

Gain spectra for the uncoated 500 μ m device have been plotted as a function of current for two temperatures in figure 3.16. In figure 3.17, the net gain spectra from the 1000 μ m uncoated device at 300K have been shifted up by the cavity loss to produce plots of modal gain. The full width half maxima (FWHM) of the gain spectra broaden at a rate of 2.4nm/mA as the injection current increases. Below threshold, the position of the peak gain blue shifts with increasing current at a rate of 1.17nm/mA. At threshold, the gain clamps and no further broadening or shifting of the peak gain

position occurs.

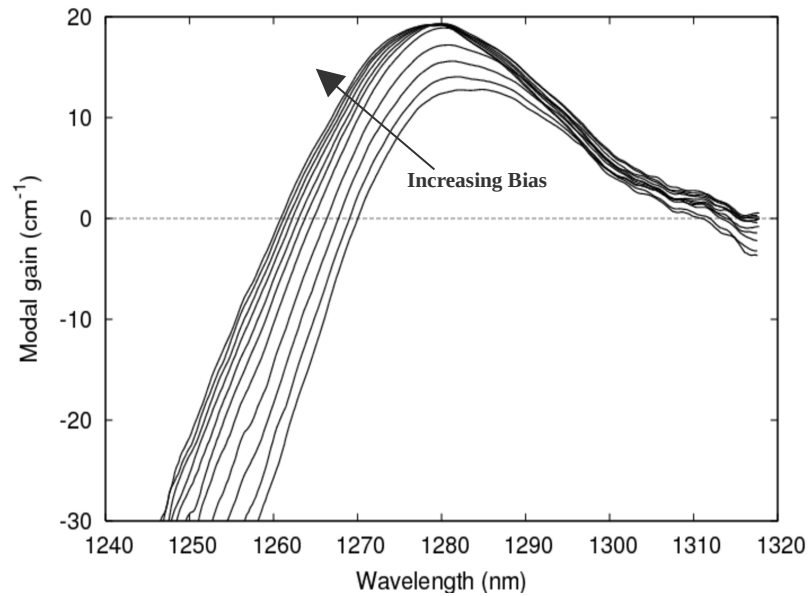


Figure 3.17: Modal gain spectra as a function of current (25mA to 35mA in 1mA steps) for the uncoated 1000 μ m device at 300K.

3.12.2 The full width half maxima of the gain spectra

The quasi-Fermi level separation and FWHM of the spectrum were extracted from each modal gain spectrum. The FWHM of the modal gain spectra of the uncoated devices is plotted against quasi-Fermi level separation in figure 3.18. As the current is increased, the quasi-Fermi level separation increases. This enables the higher energy states to lase and the FWHM of the gain spectra increases at rate of 1.23nm/meV.

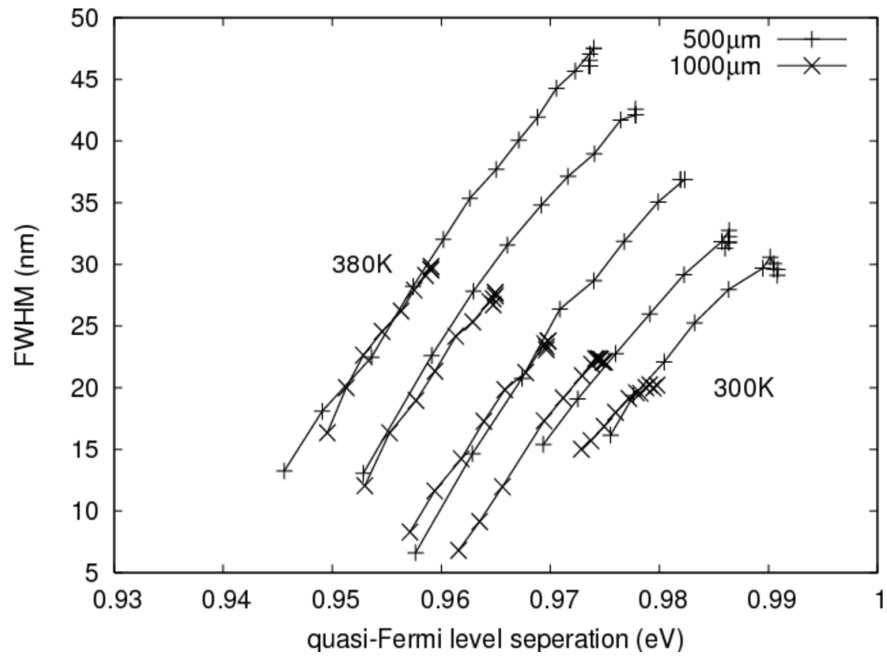


Figure 3.18: Full width half maxima of modal gain spectra plotted as a function of quasi-Fermi level separation for the 500 μm and 1000 μm uncoated devices at different temperatures.

The FWHM of the spectra have been measured up to 45nm. This is compared to a typical

FWHM in InP-based devices of 51-70nm [25]. There are two probable reasons for the smaller FWHM in dilute nitride based devices. Firstly, inhomogeneous pumping may occur, due to the large number of QWs within InGaAsP devices. Secondly, the higher conduction band effective mass of the dilute nitrides (0.0810) compared to InGaAsP (0.0584) leads to a higher density of states at the bottom of the conduction band, possibly resulting in a narrower lasing spectrum.

3.12.3 Lasing wavelength

The shift in the wavelength of the peak gain for all measured devices is shown in figure 3.19 as a function of injection current density. It can be seen from this figure that the behaviour of the peak gain for all devices is similar. This suggests that the material was homogeneous and undamaged for all of the devices investigated.

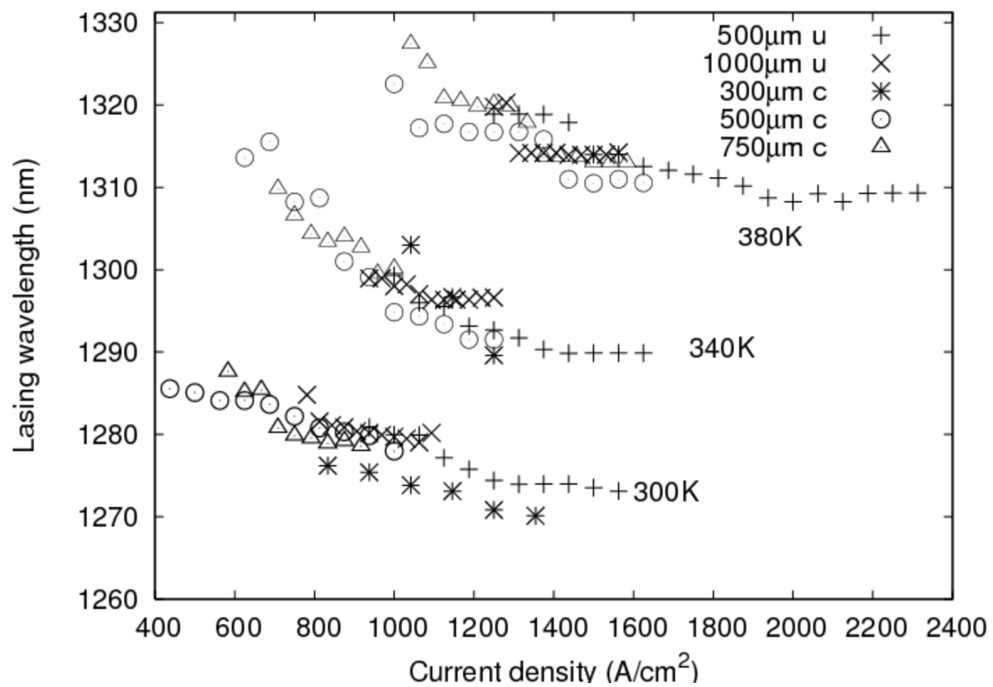


Figure 3.19: Peak gain position versus current density for coated (c) and uncoated (u) devices shown at 300K, 340K and 380K.

As in figure 3.15, the peak gain is seen to red shift as the temperature increases. This is due to band gap narrowing of the QW. The peak gain wavelength shifts at a rate of 0.41nm/K between 300K and 340K, whilst this rate increases to 0.60nm/K between 340K and 380K. This gives an average rate of 0.51nm/K. This is comparable to InP-based devices which have a typical value of 0.50nm/K [24]. As the injection current is increased, the peak gain wavelength blue shifts at a rate of 11pm A⁻¹cm² until the

modal gain clamps at threshold. This is also comparable to (if not slightly better than) the shift of $13 \text{ pm A}^{-1}\text{cm}^2$ reported for InP-based devices [25].

As the lattice temperature increases, the quasi-Fermi level separation needed to produce the same value of net gain decreases. This can be seen in figure 3.20, which plots the net gain as a function of quasi-Fermi level separation for all of the devices measured. The quasi-Fermi level separation that is required to produce the same value of net gain reduces at a rate of $\sim 0.26 \text{ meV/K}$. This is due mainly to band gap shrinkage. The band gap shrinks at a rate of $\sim 0.37 \text{ meV/K}$ (see chapter 4), which is slightly larger than the reduction in quasi-Fermi level separation. The difference is probably due to the increased carrier density and thus Fermi level separation needed to achieve the same net gain at a higher temperature.

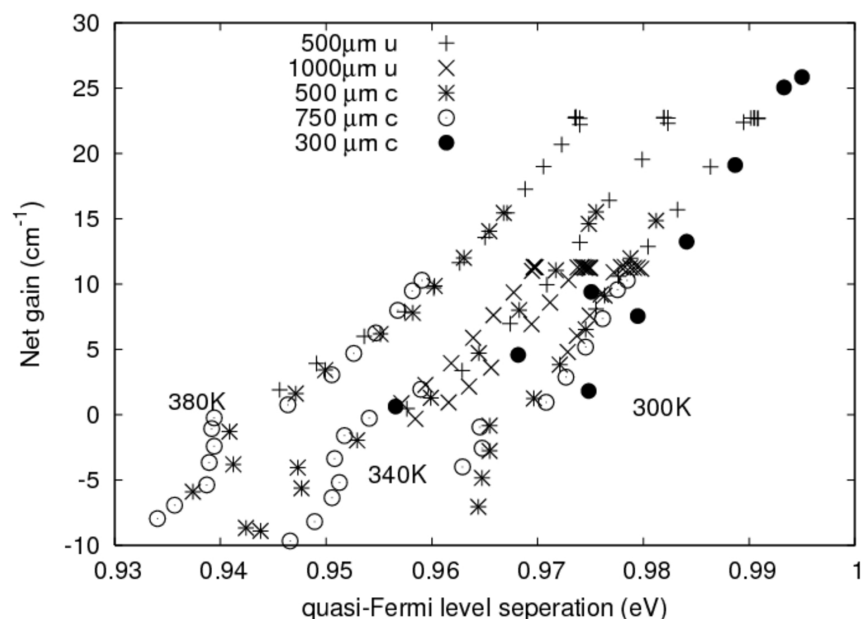


Figure 3.20: Net gain spectra versus quasi-Fermi level separation for coated (c) and uncoated (u) devices with an assumed loss of 8 cm^{-1} at 300K, 340K and 380K.

In figure 3.21, the quasi-Fermi level separation is plotted as a function of injection current and temperature for the uncoated 500 μ m device. The quasi-Fermi level separation increases at a rate of 2.85meV/mA until threshold. At this point, the quasi-Fermi levels pin and no further increase in separation is observed. The shift of the threshold current with temperature can be estimated from this graph. Between 300K and 360K an approximately linear shift of 0.10mA/K is observed. However, between 360K and 380K, the threshold current shifts more dramatically at a rate of 0.26mA/K. These correspond to characteristic temperatures of 282K and 113K, respectively. Both these values of T_0 compare very favourably with InP-based devices. (It should however be noted that InP-based devices do not work well above 360K.) The second characteristic temperature is only observed at high temperatures in shorter cavities, suggesting that it is carrier density dependent. The most probable cause of the decrease in T_0 are holes escaping from the QW via thermionic emission, although Auger processes may also play a role.

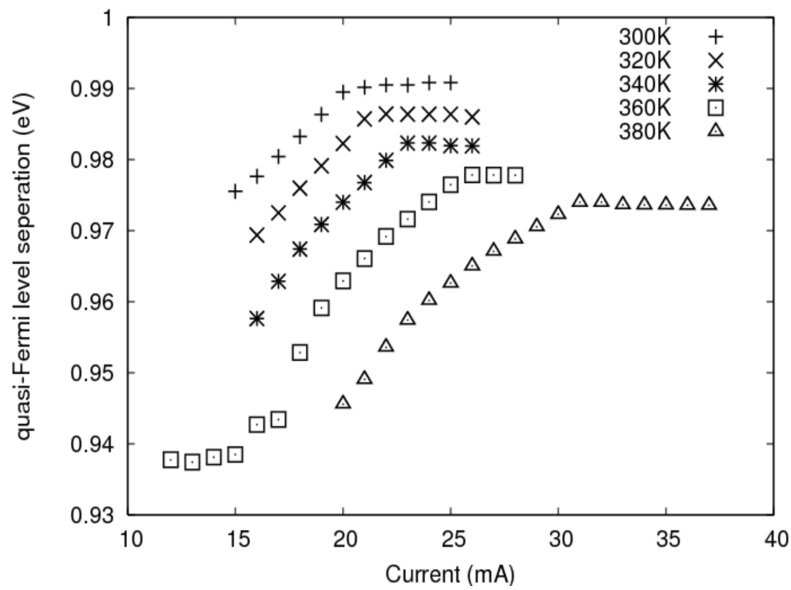


Figure 3.21: Quasi-Fermi level separation versus current for the 500 μm uncoated device at varying temperatures.

The increase in the current required to achieve threshold at higher temperatures is primarily due to the reduction of the gain caused by spread of the Fermi-Dirac distributions. However, the higher carrier densities required to achieve threshold also increase the non-radiative recombination rates.

A small, but visible kink can be seen in figure 3.21 in the below threshold curves for 340K, 360K and 380K. This kink could be attributable to an increased rate of Auger recombination at high carrier densities.

3.12.4 Extraction of effect group index and shift in effective index

Using equation 3.43, the effective group index has been extracted as a function of temperature for the 500 μm device at a constant current of 20mA. This is plotted in figure 3.22, where the shift in effective group index due only to temperature effects can be clearly seen.

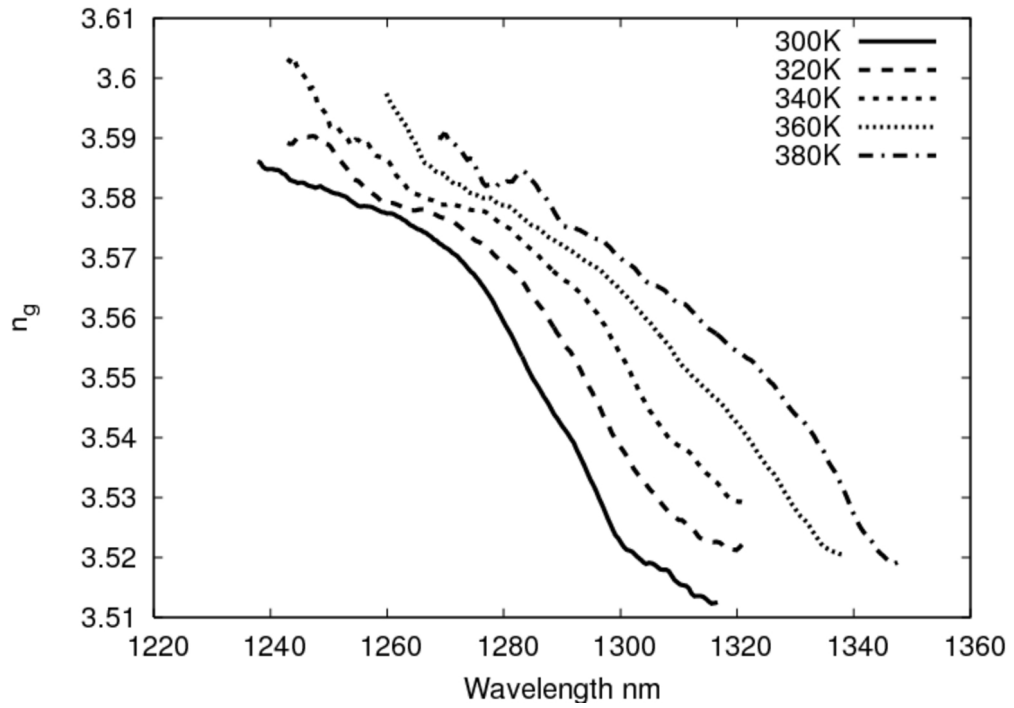


Figure 3.22: Shift of the effective group index with temperature for the 500 μ m device at a constant bias current of 20mA.

Figure 3.23 shows the shift in effective group index for increasing current at a constant temperature of 300K. The decrease in effective group index below threshold (20mA) can be clearly seen up to threshold, where the gain clamps and therefore the effective group index also clamps.

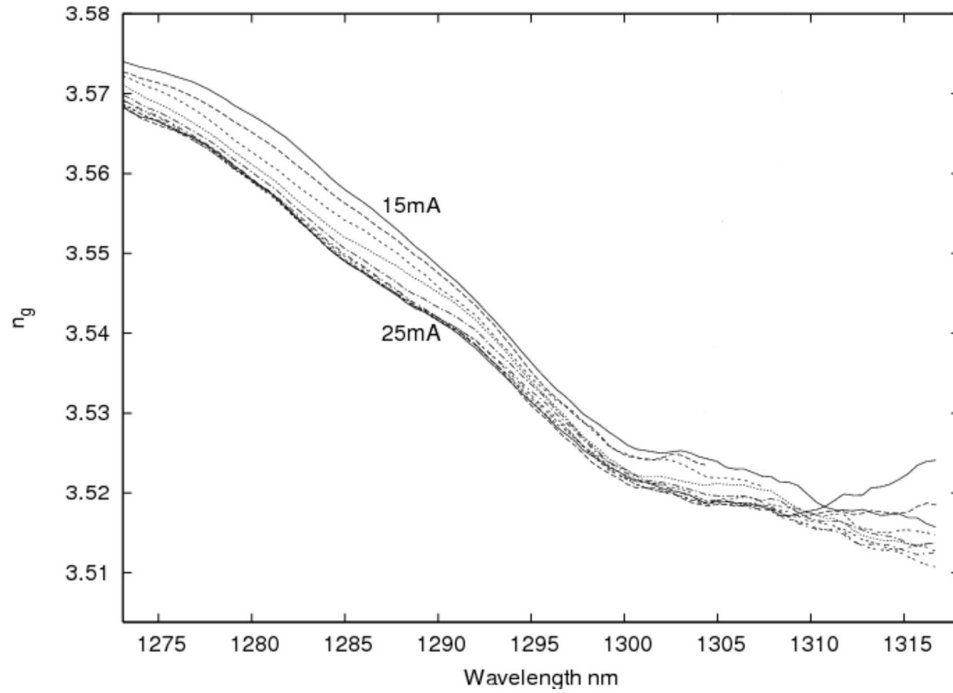


Figure 3.23: The shift of effective group index for the 500 μ m device as a function of current at 300K.

The experimental values of the group index were compared to those predicted theoretically by a 2D mode solver. The refractive index values of AlGaAs are well known and were taken from Afromowitz's work [26]. However, the refractive index of the dilute nitrides is less well known. In order to calculate the refractive index of the QWs, the simulated group index was fit to the experimental group index by varying the refractive index and dispersion ($dn_{qw}/d\lambda$) of the dilute nitride QWs. The best fit was found for a refractive index of 3.75 and a dispersion of $3 \times 10^6 \text{m}^{-1}$. Although no experimental refractive index values for $\text{Ga}_{0.613}\text{In}_{0.387}\text{N}_{0.012}\text{As}$ exist, the value obtained by fitting is consistent with the trends given in [27]. The calculated value of dispersion is higher than that measured in [27], since dispersion increases

rapidly close to the band gap of the QW (the measurement in [27] was not performed close to the band gap). Furthermore, the measurements in [27] were performed by spectroscopic ellipsometry of an unpumped surface layer, whereas our measurements were performed on QWs electrically pumped close to threshold. Jin *et al.* have previously reported on the effective group index of an InGaAsN laser [28], obtaining a higher value of 3.65. It has been reported that the refractive index increases with nitrogen content [27]. Therefore, the higher nitrogen content of 1.8% in the QW and the introduction of nitrogen into the barriers [29] could be the cause of the higher effective group index reported in [28].

The shift in effective index as a function of bias current was calculated for the 500 μm

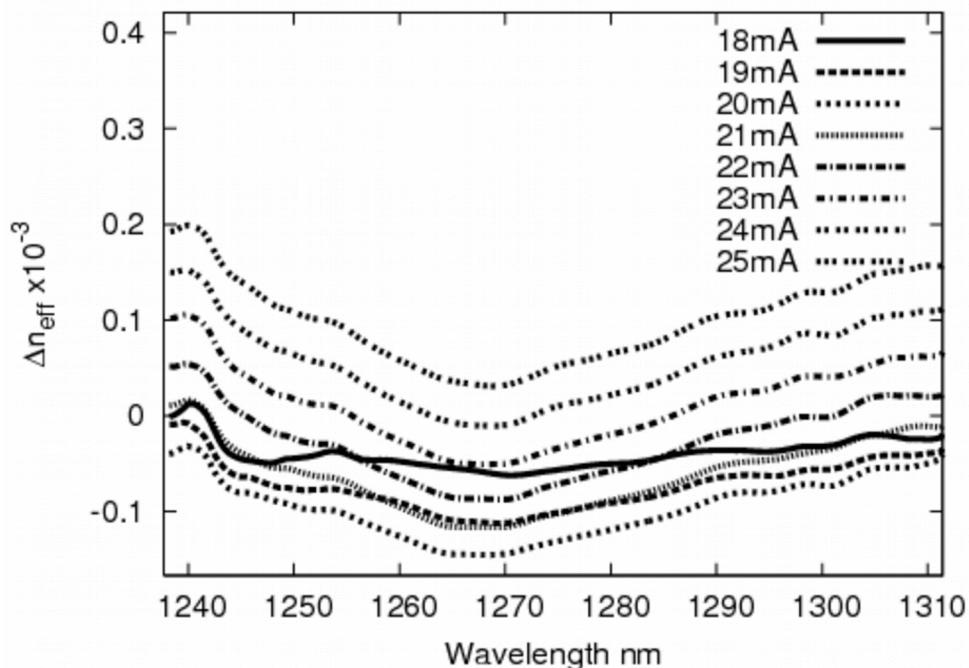


Figure 3.24: Figure : Shift in effective modal index with current for the 500 μm device. All shifts are shown relative to measurements made at 17mA.

device using equation 3.52. The results are shown in figure 3.24 and are all relative to the device operating at 17mA. Two effects can clearly be seen. As the current

increases below threshold, the gain increases so that the effective index decreases. Then, at 20mA, the gain clamps and thermal effects start to dominate. This causes the refractive index to increase again.

3.12.5 Calculation of the alpha factor

Below threshold, the changes in the effective index are dominated by the changes in the gain spectrum. However, temperature effects also play a large role. For the calculation of the alpha factor, one is interested in the change of the effective index due to the changes in gain. In this work, we follow Gerhard [29] to separate the two effects below threshold by recognising that the gain clamps at threshold, so that any changes in the effective index above threshold can be primarily attributed to thermal effects. The shift in effective index above threshold is then used to eliminate the thermally induced shift in effective index below threshold, so that only the gain induced index change remains. This method assumes that the temperature rise due to current injection is the same above and below threshold. For the 500 μ m device it was found experimentally that the effective index increased above threshold at a rate of $dn_{\text{eff}}/dI=2.55 \times 10^{-2} \text{A}^{-1}$ at 300K and at a rate of $dn_{\text{eff}}/dI=2.8376 \times 10^{-2} \text{A}^{-1}$ at 320K. These values were used to correct the effective index shift below threshold when calculating the alpha factor.

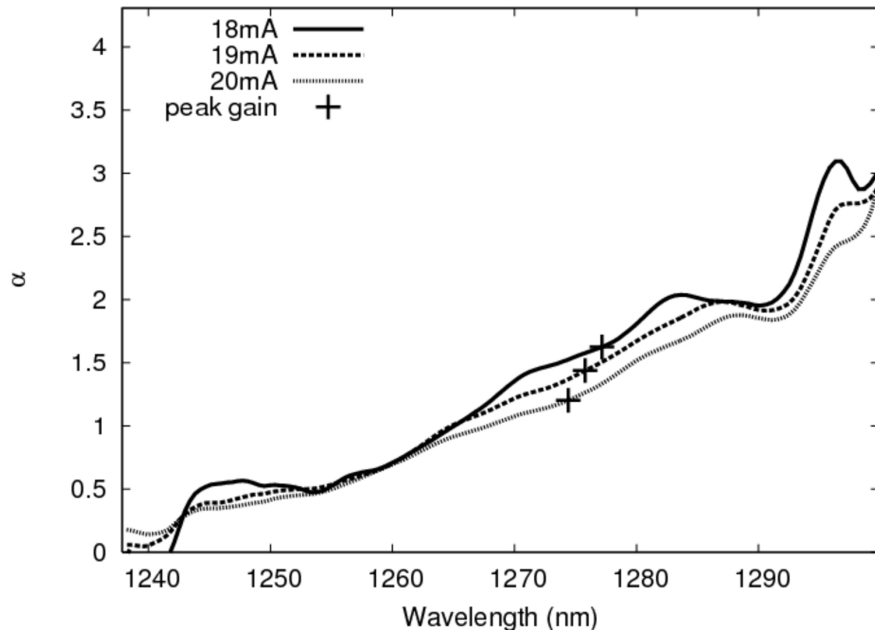


Figure 3.25: Alpha factor for the 500 μ m device plotted for 300K. The crosses represent the position of the peak gain. All values are shown relative to 17mA.

The gain and the shift in effective index have been calculated for a range of bias currents and the alpha factor was calculated from these using equation 3.54. The calculated alpha factor is plotted in figure 3.25 for the 500 μ m device at 300K. The alpha factors extracted at the peak gain position for two temperatures (300K and 320K) are plotted as a function of current density in figure 3.26.

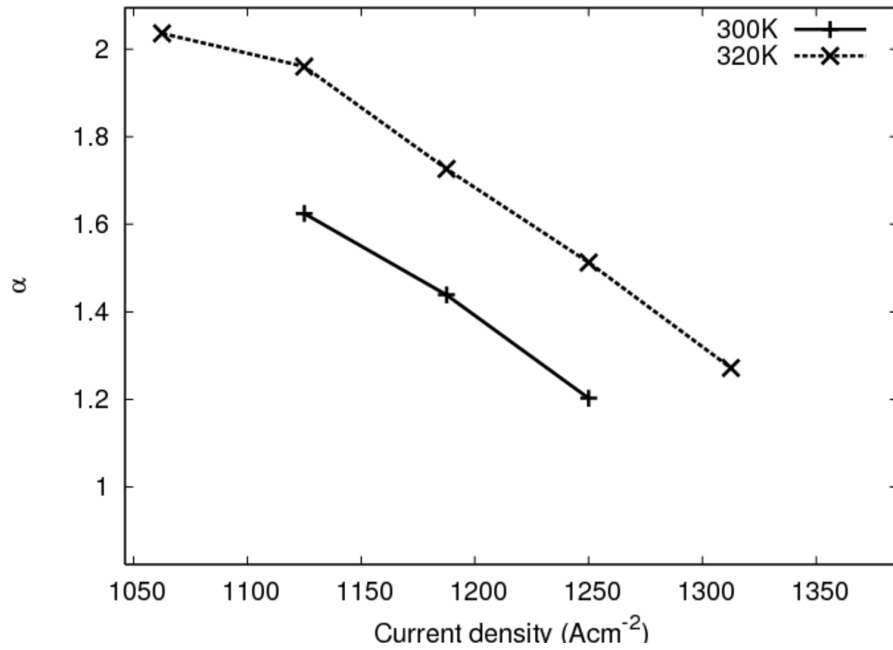


Figure 3.26: Alpha factor calculated at the position of the peak gain as a function of temperature and current density for the 500 μm device

3.12.6 Comparison of gain data against known gain spectra

Another set of devices cleaved from the same wafer as those used in this work were sent to Cardiff University pre-processed specifically for measurement with the segmented contact method [30]. As described in section 3.2, the devices measured in this work are ridge wave-guide structures. Carriers will therefore not be uniformly distributed throughout the active region due to current crowding effects and surface recombination. Thus, one would expect the results obtained by measuring these application ready devices to be significantly different to those obtained from measuring a broad area structure, with no defined cavity as used by the segmented contact method. In this section, Cardiff's measurements are compared with the data

obtained during the course of this work. Cardiff's measurements were performed at 250K, 300K, 325K and 350K whereas UNott measured at 300K, 320K, 340K, 360K and 380K. The data for 300K/300K and 320K/325K are compared as they fall closest together in terms of temperature.

Due to current spreading the exact current density in the RW structure is not known. It is therefore hard to directly compare the gain produced by the two devices as a function of carrier density.

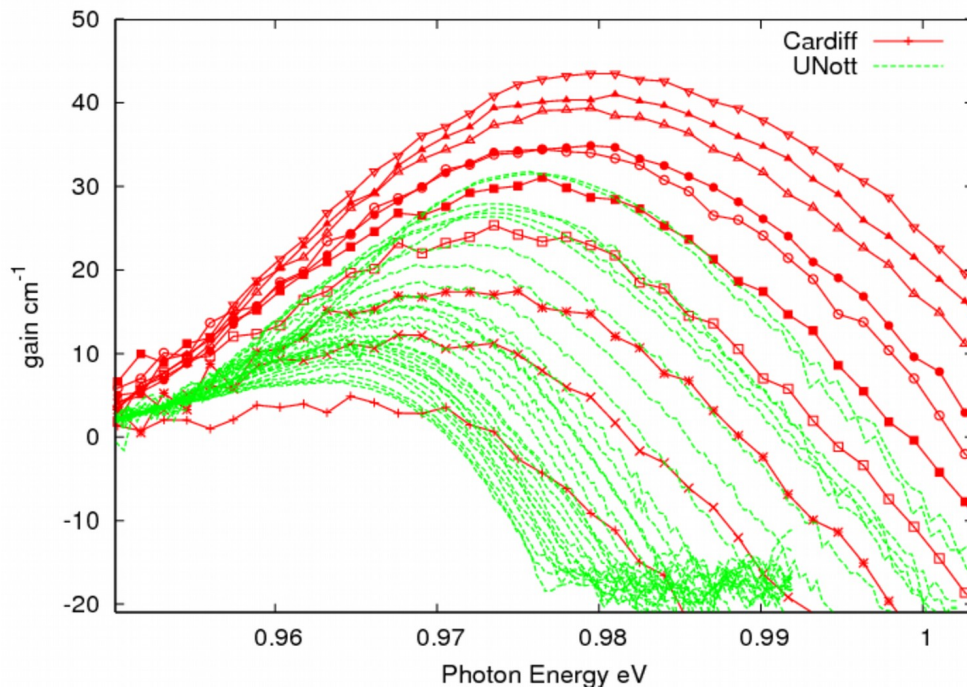


Figure 3.27: UNott's data measured from the ridge waveguide device plotted against Cardiff's data measured from the broad area device measured using the segmented contact method at 300K.

Although the exact carrier densities are not known, if the two devices have the same material gain when the low energy side of the gain curves are both aligned to the 0cm^{-1} , the curves should line up leaving any discrepancies to be examined. In figure

3.27 and 3.28 Cardiff's gain curves have been plotted against UNott's data.

Examining figure 3.27, it can be seen that the curves with high peak gain. Agree well, i.e. both the peak of the gain and the high/low energy slopes line up. The two sets of data do not compare so well at lower gain. If the high energy tail of the gain spectra is followed up to the peak gain point, it can be seen that that UNott's data gives a higher peak gain than Cardiff's data. This is the opposite from what one would expect, since Cassidy's method is well known to underestimate the peak gain due to the instrument response distorting the measured ASE spectra (see section 3.11). The curves with the very lowest gain (see figure 3.27) have a very different shape with Cardiff's curves being far flatter than UNott's data.

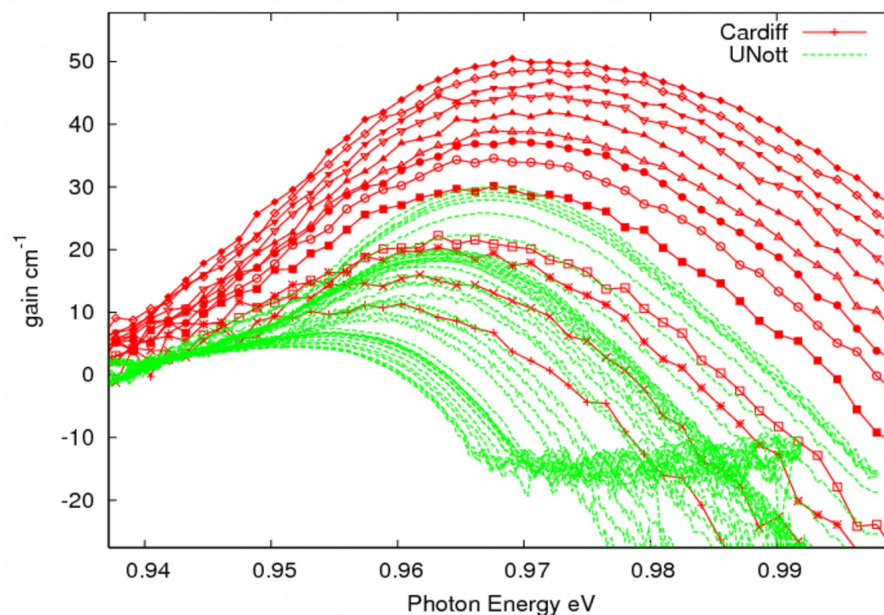


Figure 3.28: UNott's data measured from the ridge waveguide device at 320K plotted against Cardiff's data measured from the broad area device measured using the segmented contact method at 325K.

Possible reasons for the discrepancies in the measurements include

1. The confinement factor and dispersion in a ridge waveguide are significantly different to that in broad area structures. Thus, the material gain $g(x,z)$ will be multiplied by a different confinement factor in each structure. The relation relating material gain g and effective modal gain g_{eff} is given by equation 3.62, where n_a is the index of the active region

$$g_{eff}(x, z) = \frac{n_a \Gamma(x, z) g(x, z)}{n_{eff,0}(x, z)} \quad [31]. \quad (3.62)$$

This could explain the changes in slope on the high energy side of the gain spectra in the two sets of data.

2. At low gain, the signal to noise ratio of Cardiff's data appears to be poor, this brings into question the reliability of some of their lower gain curves.
3. The different processing techniques used to make the different structures, could have affected the gain characteristics - etching the ridge may have altered the material strain.
4. The devices were taken from the same wafer. However, wafers are not always uniform, so the measured material may be slightly different.
5. UNott's setup measures both the TE and TM modes, whereas Cardiff filters out the TM modes. However, there should be hardly any power in the TM mode of our RW device.

The only way to tell whether the differences in the measurements are due to the device structure or the measurement technique would be to ion-beam mill a hole through the top contact of both devices and measure the unamplified ASE spectra, and

transform this to gain. Overall it can be concluded that our measurements agree with those performed at Cardiff. However, some discrepancies at low bias have been noted which require further experimental work to determine the true cause.

3.13 Summary

In this chapter, the ASE spectra have been measured from a series of dilute nitride laser diodes with both coated and uncoated facets as a function of temperature and injection current. Cassidy's method has been used to extract the gain spectra. The error introduced due to the non-ideal spectral response of the OSA has been estimated using a combination of simulation tools and experimental measurements. The resulting estimated worst-case error is 1.0 cm^{-1} for the modal gain and 1.6 cm^{-1} for the net gain. The cavity loss has been determined to be 8 cm^{-1} . The widths of the gain spectra have been extracted as functions of quasi-Fermi level separation and temperature. The values of the peak gain decrease at a rate of $0.26 \text{ cm}^{-1}/\text{K}$ as the temperature increases, whilst the spectra red shift at a rate of $0.51 \text{ nm}/\text{K}$ due to QW band gap narrowing.

Effective group index values between 3.52-3.59 were obtained. The effective group index was extracted and fit with the group index values obtained from a 2D mode solver. The refractive index of the QW was calculated to be 3.75 with a dispersion ($dn/d\lambda$) of $3 \times 10^6 \text{ m}^{-1}$. The change in effective index was extracted and the linewidth enhancement factor was found to be between 1.87-2.84.

Finally, the gain data measured in this chapter was compared to that measured at Cardiff University using the segmented contact method. Although the gain spectra were found not to match at low bias currents, good overall agreement was found between the two sets of data.

The performance figures (T_0 , cavity losses, wavelength shift with temperature) measured in this work are comparable to, if not better than, the more traditional InP-based devices. The good thermal stability of the dilute nitride devices linked to the fact that they are grown on low cost GaAs substrates (i.e. not expensive InP) suggests that the dilute nitride material system may become a viable competitor to InP-based devices.

3.14 Further work and improvements in the measurement system

The experimental system was developed specifically to obtain the measurements presented in this chapter. During the course of the measurements, the software and hardware of the experimental system were continually optimised to provide better results and gather them more efficiently. After measuring all of the devices the system was robust and the measurement of ASE spectra had become routine. However, if more time, funding and devices were available the following things would be improved upon.

3.14.1 The optical spectrum analyser

1. If a multi-mode OSA were available it would enable the use of a 50 μm multi-

mode fibre rather than the 8 μm single mode fibre. This would improve the coupling efficiency dramatically, giving a better signal to noise ratio and shorter measurement time.

2. An OSA with a smaller FWHM would reduce the impact of the instrument response. A spectral resolution smaller than 0.01nm would be a worthwhile improvement.
3. An OSA which can sample more than 5000 points (e.g. 500000) would enable more of the gain spectrum to be sampled. This, combined with a better SNR would enable more of the high energy tail of the gain spectra to be resolved. This would make the cavity loss and the quasi-Fermi level separation easier to determine.

3.14.2 The devices

1. The devices would be wire bonded from the start to minimise the risk of damaging them.
2. Measuring coated devices was problematic because the facet reflectivity was not precisely known. It would be more useful for this type of measurement to have only uncoated devices.
3. We were provided with devices of lengths varying from 250 μm to 2000 μm . The longer devices proved problematic to measure due to the narrow mode spacing (2-1 μm) and limited spectral resolution of the OSA.
4. It would be ideal if the devices had an ion-beam milled top contact window, so that both direct and indirect methods of measuring the gain could be

performed simultaneously. This would help thus eliminate any uncertainty in the results.

5. Only one device should be mounted per heat sink. The heat sink used only had one insulated contact, thus only one device could be bonded at a time. If a device failed or a measurement from the other device were needed, the bond had to be broken and a new bond made.

3.14.3 The laboratory

1. A temperature stabilised room and a vibration isolated table would have helped stop the fiber becoming misaligned during the measurements. This was particularly problematic in summer when the room cooled/heated by up to fifteen degrees after sunset/sunrise.

3.14.4 Improvements in the software

1. Automatically finding threshold and from this automatically setting up the range of currents to be measured would be useful. This was not implemented for fear of damaging the device.

3.14.5 The measurement technique

1. A combined motorised and piezoelectric stage with feedback sensors would have sped up the measurements. As it stands, the system can only be left running over a 40 degree temperature range, thus the fibre must be realigned about three times per measurement. The piezoelectric actuators did not have

feedback, which meant one could not be certain as to whether the fibre was properly aligned.

2. A Peltier cooler should be introduced so measurements below room temperature can be performed. Although the lowest temperature measured during this set of measurements was 300K, during the summer months this temperature could only be performed at night and early in the morning.

3.15 References

- [1] S.M. Wang and A. Larsson, "High-frequency modulation and bandwidth limitations of GaInNAs double-quantum-well lasers", *Appl. Phys. Lett.*, 88, 051103, 2006.
- [2] H. Wang and D. T. Cassidy "Gain Measurements of Fabry–Pérot Semiconductor Lasers Using a Nonlinear Least-Squares Fitting Method" *IEEE J. Quant. Electron.*, 41, 4, p. 532, 2005
- [3] Basil W. Hakki and Thomas L. Paoli, "Gain spectra in GaAs double-heterostructure injection lasers", *Journal of Applied Physics* 46, 3, 1975
- [4] University of Nottingham FAST ACCESS "Low-cost 1.3 μ m sources for FAST ACCESS technologies" Milestone M11 Report on gain characterization of first dilute nitride QW (preliminary)
- [5] Daniel T. Cassidy, "Technique for measurement of the gain spectra of semiconductor diode lasers", *J. Appl. Phys*, 56, 11, p. 3096 , 1984

- [6] G. M. Lewis, P. M. Snowton, J. D. Thomson, H. D. Summers, and P. Blood, "Measurement of true spontaneous emission spectra from the facet of diode laser structures", *Appl. Phys. Lett.* 80, 1, 2002
- [7] H.C. Casey, J.P. and M.B. Panish "Heterostructure Lasers Part A: Fundamental Principles" *Quantum Electronics Principles and Applications*", ISBN: 0-12-163101-X, Academic Press Inc, 1978
- [8] E. Avrutin, I. Chebunina, I. Eliashevitch, S. Gurevich, and G. Shtengel, "TE and TM optical gains in AlGaAs/GaAs single quantum well lasers", *Semicond. Sci. Technol.* 8, 80 1993
- [9] G. Shtengel and D. Ackerman, "Internal optical loss measurements in 1.3 μm InGaAsP lasers", *Electron. Lett.* 31,14, pp.1157-1159,1995
- [10] Linzhang Wu, "Accurate determination of quasi-Fermi-level separation of semiconductor lasers", *Appl. Phys. Lett.*, 76, 8, p.964, 2000
- [11] WU Lin-Zhang, TianWei, Gao Feng, "Determination of Quasi Fermi-Level Separation of Semiconductor Lasers from Amplified Spontaneous Emission", *Chin. Phys. Lett.* 21, 7 pp.1359, 2004
- [12] Lin Zhang Wu and Heinz Schweizer Liwei Fu, "The extension of gain spectra and accurate determination of the quasi-Fermi-level separation from measured amplified spontaneous emission spectra" *Appl. Phys. Lett.*, 75, 15, p. 3069 ,1999
- [13] H.C. Casey, J.P. and M.B. Panish "Heterostructure Lasers Part A: Fundamental

Principles” Quantum Electronics Principles and Applications”, ISBN: 0-12-163101-X, Academic Press Inc, p.120 , 1978

[14] Linzhang Wua, “Accurate determination of quasi-Fermi-level separation of semiconductor lasers ”, Appl. Phys. Lett., 76, 8, p.964, 2000

[15] Agrawal and Dutta “Semiconductor Lasers Second Edittion”, ISBN: 0-442-01102-4, Van Hostrand Reinhold Press, p.33, 1993

[16] Turley, Thompson and Lovelace, “Effect of injection current on the dielectric constant of an inbuilt waveguide in twin-transverse-junction stripe lasers”, Electron. Letters, 15,9, pp. 256-257, 1979

[17] N. C. Gerhardt, M. R. Hofmann, J. Hader, J. V. Moloney, S. W. Koch, and H. Riechert , “Linewidth enhancement factor and optical gain in (GaIn)(NAs)/GaAs lasers ”, App. Pphys. Lett. , 84, pp. 1-3, 2004

[18] A. Klehr, G. Beister, G. Erbert, A. Klein, J. Maege, I. Rechenberg, J. Sebastian, H. Wenzel, and G. Tränkle, “Defect recognition via longitudinal mode analysis of high power fundamental mode and broad area edge emitting laser diodes”, J. Appl. Phys., 90, 43, 2001

[19] P.J. Bream, S. Bull, R. Xia, A.V. Andrianov, I. Harrison, and E.C. Larkins, “The influence of defects on the emission spectra of high power laser diodes”, Conference on Lasers and Electro-Optics Europe, (CLEO)/Europe, 2003

[20] H. Wang and D.T. Cassidy, ”Gain measurements of Fabry-Perot semiconductor

lasers using a nonlinear least-squares fitting method”, IEEE J. Quantum Electron., 41,4, pp. 532- 540, 2005

[21] William H. Press, Saul A. Teukolsky, William T. Vetterling, Brian P. Flannery, "Numerical Recipes in C - The Art of Scientific Computing Second Edition", ISBN 0-521-43108-5, 1997

[22] J. Wu, W. Shan and W. Walukiewicz, “Band anticrossing in highly mismatched III–V semiconductor alloys”, Semicond. Sci. Technol., 17, pp.860-869, 2002

[23] P.S. Zory Jr., “Quantum Well Lasers”, ISBN: 0127818901, Academic Press, 1993

[24] X. Zhang, J.A. Gupta, P.J. Barrios, G. Pakulski, X. Wu and A. Delage, “Gain Spectra of 1.3 μ m GaInNAs Laser Diodes”, J. Vac. Sci. Technol. A, 24, p. 787, 2006

[25] D.A. Ackerman, G.E. Shtengel, M.S. Hybertsen, P.A. Morton, R.F. Kazarinov, T. Tanbunek and R.A. Logan, “Analysis of Gain in Determining To in 1.3 μ m Semiconductor Lasers”, IEEE Selected Topics in Quantum Electron., 1, p. 250, 1995

[26] Afromowitz, M.A., ”Refractive index of Ga_{1-x}Al_xAs”, Solid State Comm., 15., pp. 59-63,1974

[27] Takeshi Kitatani, Masahiko Kondow¹, Kazunori Shinoda, Yoshiaki Yazawa and Makoto Okai, “ Characterization of the Refractive Index of Strained GaInNAs Layers by Spectroscopic Ellipsometry” Jpn. J. Appl. Phys., 37 (3A), pp.753-757, 1998

- [28] Jin, S.R., Fehse, R., Sweeney, S.J., Knowles, G., Adams, A.R., O'Reilly, E.P., Riechert, H., Illek, S., Egorov, A. Yu., Thijs, P.J.A., Uchida, T., and Fujii, T., "Modal refractive index of 1.3mm InGaAsP, AlGaInAs and GaInNAs semiconductor lasers under high hydrostatic pressure", *Electron. Lett.*, 38, 7, pp. 325 -327, 2002
- [29] Borchert, B., Egorov A. Y., Illek S., and Riechert H., "Static and Dynamic Characteristics of 1.29 μ m GaInNAs Ridge-Waveguide Laser Diodes", *IEEE Photon. Technol. Lett.*, 12, 6, pp. 597-599, 2000
- [30] P.M. Smowton, J.D. Thomson, A. George, M. Mexis, S.M. Wang, M. Sadeghi, and A. Larsson, "Temperature dependence of gain and recombination in single and double quantum well InGaNAs structures grown by MBE", *Workshop on GaInNAs: Materials, Devices, and Technology*, Cardiff, UK, April 10th, 2006
- [31] J. J. Lim, "Investigation of Factors Influencing the Brightness of High-power, High-brightness Laser Diodes", *University of Nottingham PhD Thesis*, p. 146, 2003
- [32] C. A. Green, N. K. Dutta, and W. Watson, "Linewidth enhancement factor in InGaAsP/InP multiple quantum well lasers", *A.P.L. Lett.* 50, 20, p. 1409, 1990
- [33] W. Rideout, B. Yu, J. LaCourse, P. K York, K. J. Beernink, and J. J. Coleman, "Measurement of the carrier dependence of differential gain, refractive index, and linewidth enhancement factor in strained-layer quantum well lasers", *Appl. Phys. Lett.* 56 (8) p. 706
- [34] N. K. Dutta, J. Wynn, D. L. Sivco, and A. Y. Cho, "Linewidth enhancement

factor in strained quantum well lasers”, Appl. Phys. Lett. 56 (23) p. 2293 ,1990

[35] N. K. Dutta, J. Wynn, D. L. Sivco, and A. Y. Cho, “Linewidth enhancement factor in strained quantum well lasers”, Appl. Phys. Lett. 57, 14, p. 1390 , 1990

[36] L. F. Tiemeijer, P. J. A. Thijs, P. J. de Waard, J. J. M. Binsma, and T. v. Dongen, “Dependence of polarization, gain, linewidth enhancement factor, and K factor on the sign of the strain of InGaAs/InP strained-layer multiquantum well lasers”, Appl. Phys. Lett. 58,24, p. 2738 , 1991

[37] L. F. Tiemeijer, P. J. A. Thijs, P. J. de Waard, J. J. M. Binsma, and T. v. Dongen, “Dependence of polarization, gain, linewidth enhancement factor, and K factor on the sign of the strain of InGaAs/InP strained-layer multiquantum well lasers”, Appl. Phys. Lett. 58,24, p. 2738 , 1991

[38] Woon-Ho Seo and John F. Donegan, “Linewidth enhancement factor of lattice-matched InGaNAs/GaAs quantum wells”, Appl. Phys. Lett. ,82, 4 p.505 , 2003